

Double, triple, and quadruple magic wavelengths for cesium ground, excited, and Rydberg states

A. Bhowmik,^{1,2,*} M. Gaudesius,^{1,2} G. Biedermann,^{1,2} and D. Blume^{1,2,†}

¹*Homer L. Dodge Department of Physics and Astronomy,
The University of Oklahoma, Norman, Oklahoma 73019, USA*

²*Center for Quantum Research and Technology, The University of Oklahoma, Norman, Oklahoma 73019, USA*
(Dated: June 4, 2024)

Dynamic polarizabilities of cesium Rydberg states, explicitly $nS_{1/2}$, $nP_{1/2}$, $nP_{3/2}$, $nD_{3/2}$, and $nD_{5/2}$, where the principal quantum number n is 40 to 70, are presented for linearly polarized light. The dynamic polarizability is calculated using the sum-over-states approach. We identify double magic wavelengths in the range of 1,000 – 2,000 nm for simultaneous trapping of the ground state and a Rydberg state, which are, respectively, red-detuned and blue-detuned with respect to a low-lying excited auxiliary state. Based on calculations of the radiative lifetime, blackbody radiation induced transitions, and population transfer out of the Rydberg and auxiliary states (estimated within two-state as well as master equation models), we conclude that magic wavelength trapping is particularly promising experimentally for the $nD_{J,|M_J|}$ Rydberg series with angular momentum $J = 3/2$ and projection quantum numbers $M_J = \pm 1/2$ (auxiliary state $8P_{1/2}$) and $M_J = \pm 3/2$ (auxiliary state $8P_{3/2}$), using trap depths as large as 10 μ K. Moreover, by tuning the angle between the quantization axis and the polarization vector of the light, we identify triple and quadruple magic wavelengths, for which the polarizabilities of the ground state, a Rydberg state, and, respectively, one and two low-lying excited states are equal. Our comprehensive theoretical study provides much needed guidance for on-going experimental efforts on cesium Rydberg-state based quantum simulations that operate on time scales up to several μ s.

I. INTRODUCTION

An excited atomic state with a high principal quantum number n is referred to as a Rydberg state. Rydberg states have intriguing characteristics such as a large size, large transition dipole moments, strong controllable long-range interactions [1], and long lifetimes [2]. These properties are being leveraged in a range of applications across various branches of physics. Specifically, Rydberg atoms constitute an appealing platform for quantum logic devices [3–5], quantum information protocols [6], quantum computing [7], quantum signal processing [8], quantum simulations [9], investigations of fundamental few- and many-body physics questions [10–13], nonlinear quantum optics [14], and so-called transmission imaging [15].

The radiative lifetime of a Rydberg atom scales with the principal quantum number as n^3 [2]. For $n \approx 50$, the lifetime is typically of the order of 100 μ s, which is much longer than the radiative lifetime of, e.g., low-lying excited states of alkali atoms. The radiative lifetime of a Rydberg state may, however, be significantly reduced by blackbody radiation induced population transfer out of the Rydberg state [16], thereby potentially placing strict limits on the length of experimental Rydberg-atom based quantum information processing and quantum simulation protocols [17–19].

Rydberg lifetime calculations are not only important from experimental and quantum technology points of

view, but also from a theory point of view. Since a state's lifetime is governed by a set of matrix elements and transition wavelengths, accurate lifetime determinations can be used to benchmark other quantities such as the atomic polarizability [20, 21]. In this work, we calculate the spontaneous lifetime, blackbody radiation lifetime, and effective lifetime of several ¹³³Cs Rydberg series, namely the $nS_{1/2}$, $nP_{1/2}$, $nP_{3/2}$, $nD_{3/2}$, and $nD_{5/2}$ series with $n \in [40, 70]$. These lifetimes play an important role in assessing the experimental feasibility of simultaneously trapping ground state and Rydberg states at so-called magic wavelengths; their determination and interpretation are the main topic of this paper.

In most cold atom experiments, ground state atoms are trapped by employing a far-off-resonant red-detuned optical-dipole trap [22]. The reason is that the polarizability of the ground state is positive when the light is red detuned with respect to a low-lying transition line, thereby creating an attractive force for the ground state. A Rydberg atom cannot, in general, be held in place with this set-up since the linearly polarized light creates a repulsive force for the Rydberg state, owing to the Rydberg states' negative "background polarizability" [23]. In addition to resulting in anti-trapping, excitation of an atom to a Rydberg state may induce heating and decoherence due to entanglement of the spin and motional states [24]. In experiments that use a red-detuned optical dipole trap for the ground state, the heating is minimized by turning the trapping laser off while the atom resides in the Rydberg state [3]. For some applications, including quantum simulation studies, it is, however, desirable to keep the atom trapped while it resides in a Rydberg state.

Several avenues for trapping Rydberg atoms have been

* anal.bhowmik-1@ou.edu

† doerte.blume-1@ou.edu

pursued. ^{87}Rb Rydberg atoms were trapped experimentally in a one-dimensional ponderomotive optical lattice by repeatedly reversing the lattice potential on a time scale that is fast compared to the lifetime of the Rydberg state [25]. Ensembles of ^{87}Rb Rydberg atoms have also been trapped in a one-dimensional optical lattice [26]. A ponderomotive bottle beam trap was used to demonstrate three-dimensional trapping of ^{87}Rb Rydberg atoms in the states $nS_{1/2}$, $nP_{1/2}$, and $nD_{3/2}$ with $60 \leq n \leq 90$ [27]. Since bottle beam traps are comparatively challenging to create experimentally [27, 28], the quest for alternative Rydberg state trapping protocols is ongoing. Very recently, e.g., the ground state and Rydberg state of a neutral ytterbium atom were trapped simultaneously in a single frequency optical tweezer trap, which confines the ground state (standard red-detuned dipole trap), by utilizing the polarizability of the ionic core [29]. This approach is restricted to huge Rydberg states since the outer electron must reside in the region where the light intensity is negligible so that the positive polarizability of the ionic core is not "overshadowed" by the negative polarizability of the valence electron.

Alternatively, it was proposed in 1999 that the ground state and a Rydberg state could be trapped simultaneously at magic wavelengths for which the differential ac-Stark shift of the two states is cancelled [30]. Even though magic wavelengths are nowadays used routinely in cold atom experiments (see, e.g., Ref. [31] for a discussion of the use of magic wavelengths in quantum metrology), their use in the context of Rydberg experiments is still comparatively rare [32–34].

Building on Refs. [35, 36], we carefully investigate a scheme for simultaneously trapping the cesium ground state and a Rydberg state in an attractive potential well at magic wavelengths for which the ground state is red-detuned and the Rydberg state is blue-detuned. Our calculations of the dynamic polarizability, which governs the trapping force, assume a linearly polarized Gaussian-shaped light beam. In this scheme, the Rydberg state is trapped thanks to the admixture of an auxiliary state. Light scattering and transitions out of the two-state manifold formed by the ground state and the Rydberg state, which can severely compromise the usefulness of the scheme, are analyzed. A comparatively high light intensity, e.g., guarantees trapping (this is our aim) but also enhances the likelihood of unwanted transitions to the auxiliary state. The $nD_{3/2, |M_J|}$ series with projection quantum numbers $M_J = \pm 1/2$ and $\pm 3/2$ are found to be the most promising candidates for magic wavelength trapping.

Moreover, we identify several triple magic wavelengths at which not only the ground state and a Rydberg state are trapped (referred to as double magic wavelengths) but also an additional low-lying excited state, which we refer to as an intermediate state. Triple magic wavelengths were, e.g., also found for ytterbium and cadmium [37, 38]. Lastly, we also identify a number of quadruple magic wavelengths, at which the

ground state, the Rydberg state, and two intermediate states are trapped simultaneously. The identified triple and quadruple magic wavelengths provide exciting new prospects for Rydberg state physics.

The remainder of this paper is organized as follows. Section II presents the radiative, blackbody, and effective lifetimes of Rydberg states. Section III presents the static and dynamic polarizabilities for several cesium Rydberg series. From the dynamic polarizabilities, we extract double magic wavelengths as a function of n for various auxiliary states. Section IV assesses the experimental realizability of the magic wavelength based trapping scheme by analyzing the Rabi frequency and the transition probability between the Rydberg and auxiliary states. Section V presents triple and quadruple magic wavelengths and the corresponding polarizabilities. The paper ends with conclusions in Sec. VI. Technical details are relegated to appendices. The supplemental material tabulates a large number of magic wavelengths and their characteristics as a function of n .

II. LIFETIME OF RYDBERG STATES

The spontaneous lifetime τ_{SP} of the k -th atomic state is calculated from the radiative transition probability via [39]

$$\tau_{\text{SP}} = \frac{1}{\sum_i A_{ki}}, \quad (2.1)$$

where A_{ki} is the transition probability from the k -th state to the i -th state. The sum runs over all states i with $E_i < E_k$, where E_i and E_k denote the energies of the i -th and the k -th states, respectively. Throughout this work, the transition probabilities account only for the strongest transitions, namely the dipole transitions [39]:

$$A_{ki} = \frac{4\alpha\omega_{ki}^3}{3c^2(2J_k + 1)} |\langle \psi_k || d || \psi_i \rangle|^2. \quad (2.2)$$

Here, α denotes the fine structure constant, c the speed of light in vacuum, J_k the total electronic angular momentum of the k -th state, ω_{ki} the transition frequency, and $|\langle \psi_k || d || \psi_i \rangle|$ the magnitude of the reduced electric dipole matrix element between the unperturbed atomic states ψ_k and ψ_i (d is equal to the z -component of the position vector of the electron).

As the energy difference between two adjacent Rydberg states falls within the microwave frequency range, the lifetime of a Rydberg state can be drastically modified by the blackbody radiation (BBR) photons of the microwave background field at room temperature [40], leading to an increased effective decay rate. The BBR lifetime τ_{BBR} of an atomic state can be accurately parameterized by introducing the dimensionless scaling coefficients A , B ,

C , and D [16]:

$$\tau_{\text{BBR}} = \frac{(n - \delta_{L,J})^D \exp\left(\frac{315780B}{(n - \delta_{L,J})^C(T/\text{K})}\right) - 1}{A} \text{ s} \quad (2.3)$$

(here, the temperature needs to be provided in Kelvin and the equation yields the lifetime in seconds); the values of A , B , C , and D for cesium [16] are collected in Table I for completeness. In Eq. (2.3), $\delta_{L,J}$ denotes the quantum defect parameter, whose values are reported in Appendix A. Since $\delta_{L,J}$ depends on the orbital angular momentum L and the total angular momentum J of the valence electron, τ_{BBR} depends on n , L , and J . In what follows, we report τ_{BBR} at $T = 300$ K.

TABLE I. Dimensionless scaling coefficients A , B , C , and D for cesium. The values are taken from Ref. [16].

Rydberg series	A	B	C	D
$nS_{1/2}$	0.123	0.231	2.517	4.375
$nP_{1/2}$	0.041	0.072	1.693	3.607
$nP_{3/2}$	0.038	0.056	1.552	3.505
$nD_{3/2}$	0.038	0.076	1.790	3.656
$nD_{5/2}$	0.036	0.073	1.770	3.636

Combining τ_{SP} and τ_{BBR} , the effective lifetime τ_{eff} of a Rydberg state becomes [40]

$$\frac{1}{\tau_{\text{eff}}} = \frac{1}{\tau_{\text{SP}}} + \frac{1}{\tau_{\text{BBR}}}. \quad (2.4)$$

We note that the aforementioned lifetimes depend on n , L , and J but not on M_J . Correspondingly, the Rydberg series are labeled by nL_J in this section. Columns 2-4 in Table II report the BBR, spontaneous, and effective lifetimes for selected n between 40 and 70 for the Rydberg series $nS_{1/2}$, $nP_{1/2}$, $nP_{3/2}$, $nD_{3/2}$, and $nD_{5/2}$. The good agreement between our τ_{eff} and theoretical and experimental literature values (column 5 of Table II) validates our calculations.

Squares, circles, and triangles in Fig. 1 show the BBR, spontaneous, and effective lifetimes for the Rydberg series $nS_{1/2}$, $nP_{1/2}$, $nP_{3/2}$, $nD_{3/2}$, and $nD_{5/2}$ as a function of n . All three lifetimes are observed to increase with increasing n . For the n considered, τ_{SP} and τ_{BBR} cross for the $nS_{1/2}$ series (the crossing occurs at $n = 45$) but not for the other series. For the $nP_{1/2}$ and $nP_{3/2}$ series, τ_{SP} is larger than τ_{BBR} for the range of n considered. Conversely, for the $nD_{3/2}$ and $nD_{5/2}$ series, τ_{BBR} is larger than τ_{SP} for the range of n considered. It is well-known that the spontaneous lifetime of Rydberg states increases as n^3 [2]. Since the quantum defect is small, one finds $n^3 \approx (n_{\text{eff}})^3$, where the effective principal quantum number n_{eff} is defined in Eq. (A2). The room temperature BBR photons lead to a decrease of the Rydberg atom lifetime and a modification of the scaling law. Fitting our numerical results for $n \in [40, 70]$, we find that

the scaling laws for the $nS_{1/2}$, $nP_{1/2}$, $nP_{3/2}$, $nD_{3/2}$, and

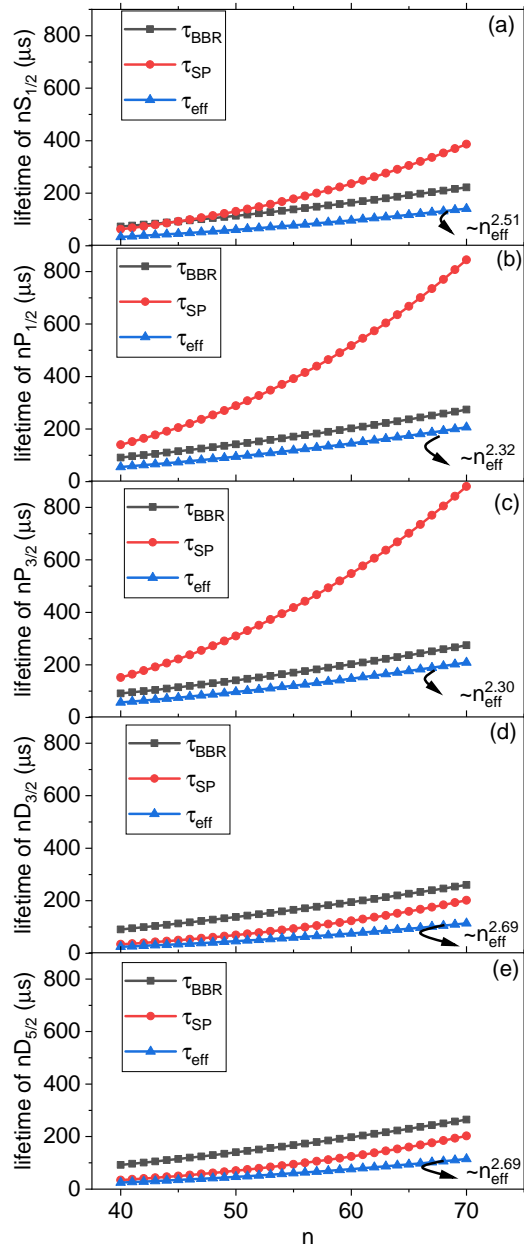


FIG. 1. Blackbody radiation lifetime τ_{BBR} , spontaneous lifetime τ_{SP} , and effective lifetime τ_{eff} for the Rydberg series (a) $nS_{1/2}$, (b) $nP_{1/2}$, (c) $nP_{3/2}$, (d) $nD_{3/2}$, and (e) $nD_{5/2}$ (the Rydberg states are labeled by nL_J). The scaling of τ_{eff} with n_{eff} is shown in each panel.

$nD_{5/2}$ series become $\tau_{\text{eff}} \propto (n_{\text{eff}})^{2.51}$, $(n_{\text{eff}})^{2.32}$, $(n_{\text{eff}})^{2.30}$, $(n_{\text{eff}})^{2.69}$, and $(n_{\text{eff}})^{2.69}$, respectively. This shows that the $nP_{1/2}$ and $nP_{3/2}$ states exhibit, among the Rydberg series considered, the largest scaling law changes due to the BBR photons.

TABLE II. Blackbody radiation lifetime τ_{BBR} , spontaneous lifetime τ_{SP} , and effective lifetime τ_{eff} for selected Rydberg states. The effective lifetimes τ_{eff} are compared to literature data (see column 5). Entries marked by the superscript a are taken from Ref. [16] while those marked by b (c) are theoretical (experimental) data taken from Ref. [41].

state	τ_{BBR} (μs)	τ_{SP} (μs)	τ_{eff} (μs)	τ_{eff} (μs) (other)
$40S_{1/2}$	72.859	62.679	33.693	33.032^a
$50S_{1/2}$	114.170	130.885	60.979	60.414^a
$60S_{1/2}$	164.091	236.301	96.842	$97.082^a, 95.2^b, 95.4 \pm 2.7^c$
$70S_{1/2}$	222.360	387.026	141.223	$143.28^a, 139.1^b, 138.6 \pm 2.4^c$
$40P_{1/2}$	91.728	140.467	55.505	55.491^a
$50P_{1/2}$	141.683	288.971	95.130	95.070^a
$60P_{1/2}$	202.501	517.278	144.830	145.53^a
$70P_{1/2}$	273.989	844.637	205.970	206.88^a
$40P_{3/2}$	91.031	152.193	57.260	56.961^a
$50P_{3/2}$	141.012	310.208	97.152	96.944^a
$60P_{3/2}$	202.219	547.844	147.230	147.70^a
$70P_{3/2}$	274.543	879.678	208.860	209.24^a
$40D_{3/2}$	90.622	34.063	24.823	24.757^a
$50D_{3/2}$	137.857	69.288	46.222	46.112^a
$60D_{3/2}$	194.589	123.603	75.604	75.589^a
$70D_{3/2}$	260.565	201.756	113.853	113.71^a
$40D_{5/2}$	92.107	34.402	25.011	25.047^a
$50D_{5/2}$	140.032	69.856	46.595	46.606^a
$60D_{5/2}$	197.583	124.407	76.252	$76.34^a, 76.3^b, 75.7 \pm 0.7^c$
$70D_{5/2}$	264.503	202.710	114.650	$114.76^a, 114.1^b, 115.4 \pm 2.2^c$

III. POLARIZABILITY AND DOUBLE MAGIC WAVELENGTHS FOR LINEARLY POLARIZED LIGHT

The dynamic electric-dipole polarizability $\alpha_v(\omega)$ (or dynamic polarizability in what follows) describes the response of the single-valence state v to an external electric field of magnitude E and angular frequency ω . Assuming a Gaussian shaped laser beam, a positive dynamic polarizability indicates an attractive force (i.e., trapping) while a negative dynamic polarizability indicates a repulsive force (i.e., anti-trapping). Throughout this section, we are interested in determining so-called double magic wavelengths $\lambda^{(d)}$ at which the cesium ground state and a Rydberg state experience the same negative Stark shifts, i.e., the same positive dynamic polarizabilities.

To determine $\alpha_v(\omega)$, we decompose it into the core polarizability $\alpha_v^C(\omega)$, the valence-core polarizability $\alpha_v^{VC}(\omega)$, and the valence polarizability $\alpha_v^V(\omega)$,

$$\alpha_v(\omega) = \alpha_v^C(\omega) + \alpha_v^{VC}(\omega) + \alpha_v^V(\omega). \quad (3.1)$$

We find that $\alpha_v^C(\omega)$ is essentially frequency-independent [$\alpha_v^C(\omega) \approx 16.12$ a.u.] while $\alpha_v^{VC}(\omega)$ is, to a good approximation, zero for all Rydberg states considered in this work; see Appendix B for details. The valence polarizability $\alpha_v^V(\omega)$ for linearly polarized light consists of the scalar component $\alpha_{v,J}^{(0)}(\omega)$ and the tensor component

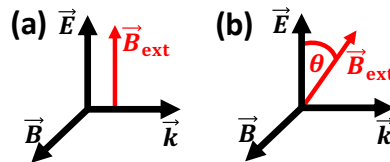


FIG. 2. Definition of the angle θ . In (a), the external magnetic field vector \vec{B}_{ext} lies along the electric field vector \vec{E} (polarization vector); this corresponds to $\theta = 0$. In (b), the angle θ between \vec{B}_{ext} and \vec{E} is finite. Section V discusses polarizability control through variation of θ .

$\alpha_{v,J}^{(2)}(\omega)$. Note that $\alpha_{v,J}^{(2)}(\omega)$ vanishes for the $nL_{1/2}$ Rydberg series. In this section, the external magnetic field \vec{B}_{ext} , which sets the quantization axis, and the polarization direction lie along the z -axis [see Fig. 2(a)]. This implies that the angle θ , which enters into the tensor polarizability [see Eq. (B3)], is zero; the ability to vary θ will be exploited in Sec. V to identify triple and quadruple magic wavelengths. The theoretical framework, implementation, and computational details to determine the energies, wavefunctions, dipole matrix elements, and polarizabilities are presented in Appendices A-B.

To benchmark our results, Table III compares the static (i.e., $\omega = 0$) scalar and tensor polarizabilities,

which are independent of M_J , for selected nL_J Rydberg states. Our results agree well with theoretical results from Ref. [35], which calculated the polarizabilities—as we (see Appendix A)—using the Coulomb approximation method. Table III also presents a comparison with experimental data from three different references. The static scalar polarizability of $1.84 \pm 0.02 \times 10^{12}$ a.u. for the $70S_{1/2}$ Rydberg state from a very recent paper [34] agrees within three sigma with our result of 1.91×10^{12} a.u.. Of the combined six experimental data from 1995 [42] and 2014 [43], one agrees with our theoretical prediction within error bars while the others deviate by between two and six sigma. Given that the polarizabilities reported in Table III vary over three orders of magnitude, we interpret the rough agreement as a validation of our theoretical predictions despite the fact that the theory-experiment agreement is not perfect.

Figure 3 shows the static scalar and tensor polarizabilities as a function of n . The static scalar polarizabilities for the $nS_{1/2}$, $nP_{1/2}$, and $nP_{3/2}$ series are positive while those for the $nD_{3/2}$ and $nD_{5/2}$ series are negative. The static scalar polarizability for the $nS_{1/2}$ series varies weakly with n compared to the other Rydberg series considered. Similar behavior was observed in Ref. [35]. The static scalar and tensor polarizabilities of the nP - and nD -series scale approximately as n^7 . The static tensor polarizabilities are negative for the $nP_{3/2}$ series and positive for the $nD_{3/2}$ and $nD_{5/2}$ series; recall that the tensor polarizability is zero for the series with $J = 1/2$.

We now turn to the dynamic (i.e., $\omega \neq 0$) polarizabilities for the $nS_{1/2,|M_J|}$, $nP_{1/2,|M_J|}$, $nP_{3/2,|M_J|}$, $nD_{3/2,|M_J|}$, and $nD_{5/2,|M_J|}$ Rydberg series. Note that since the dynamic polarizabilities depend on $|M_J|$, the labeling of the Rydberg series includes the $|M_J|$ subscript. The background polarizability of a Rydberg state, i.e., the polarizability away from resonant transition frequencies (see below), is approximately $-e^2/(m_e\omega^2)$ [23], where e and m_e are the charge and mass of the electron, respectively. Therefore, in general, the Rydberg atom is pushed toward the low-intensity region of the Gaussian beam. This implies that a conventional trap, which operates with far-off-resonant red-detuned light for the ground state, is seen as an attractive potential well for the ground state but as a repulsive potential barrier for the Rydberg state. Thus, simultaneous trapping of the ground and Rydberg states by the conventional approach is impossible. A possible solution is to create a red-detuned trap for the

ground state with a wavelength that is blue-detuned and very close to the resonance transition between the Rydberg state and an auxiliary state [36]. Since we are, motivated by experimental considerations, interested in trapping light with wavelengths between around 1,000 and 2,000 nm, the number of auxiliary states is restricted to low-lying excited states. The auxiliary states considered in this work (see Table IV) are connected to the ground state and a Rydberg state via dipole transitions for linearly polarized light ($|\Delta L| = 1$; $|\Delta J| = 0, 1$; and $\Delta M_J = 0$). While there exist lasers that operate in the

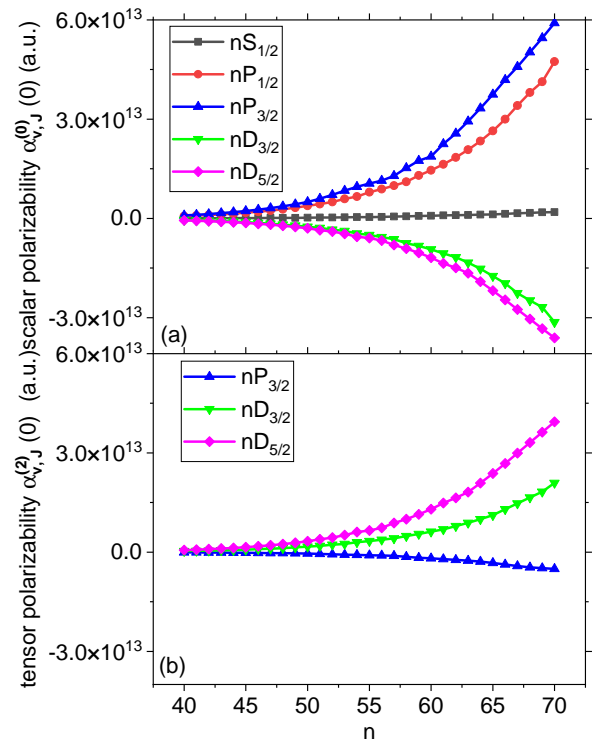


FIG. 3. (a) Static scalar polarizability $\alpha_{v,J}^{(0)}$ (a.u.) for the $nS_{1/2}$, $nP_{1/2}$, $nP_{3/2}$, $nD_{3/2}$, and $nD_{5/2}$ series and (b) static tensor polarizability $\alpha_{v,J}^{(2)}$ (a.u.) for the $nP_{3/2}$, $nD_{3/2}$, and $nD_{5/2}$ series as a function of n .

500 – 1,000 nm wavelength regime, this wavelength window is excluded from our analysis since the magic wavelengths found in this wavelength regime possess negative polarizabilities [see also Fig. 4(b)].

To make the discussion concrete, Fig. 4 considers the $6S_{1/2,|1/2|}$ ground state and the $45S_{1/2,|1/2|}$ Rydberg state. Four auxiliary states, namely $7P_{1/2,|1/2|}$, $7P_{3/2,|1/2|}$, $8P_{1/2,|1/2|}$, and $8P_{3/2,|1/2|}$, have transition wavelengths between 1,000 nm and 2,000 nm (see black numbers in Fig. 4). To illustrate the emergence of double magic wavelengths, Fig. 5(a) shows the polarizability

of the ground state and the $45S_{1/2,|1/2|}$ Rydberg state in the vicinity of the $45S_{1/2,|1/2|} - 7P_{3/2,|1/2|}$ resonance. While the polarizability of the ground state is essentially constant on the scale shown, the polarizability of the $45S_{1/2,|1/2|}$ Rydberg state changes sign at the resonance with the $7P_{3/2,|1/2|}$ auxiliary state [black vertical line in Fig. 5(a)]. The two polarizability curves cross

TABLE III. Static scalar polarizability $\alpha_{v,J}^{(0)}(0)$ and static tensor polarizability $\alpha_{v,J}^{(2)}(0)$ are compared with theoretical and experimental results from the literature for $n = 40, 50, 60$, and 70 . The polarizabilities are reported in atomic units (a.u.) in the format $x[y]$, which stands for $x \times 10^y$. Entries marked by the superscripts a, b, c , and d are taken from Ref. [35] (theoretical data), Ref. [43] (experimental data), Ref. [42] (experimental data), and Ref. [34] (experimental data), respectively.

n	scalar polarizability $\alpha_{v,J}^{(0)}(0)$					tensor polarizability $\alpha_{v,J}^{(2)}(0)$		
	$S_{1/2}$	$P_{1/2}$	$P_{3/2}$	$D_{3/2}$	$D_{5/2}$	$P_{3/2}$	$D_{3/2}$	$D_{5/2}$
40	4.27[10]	6.96[11]	9.14[11]	-4.71[11]	-5.67[11]	-8.06[10]	3.15[11]	6.30[11]
	4.27[10] ^a	6.96[11] ^a	9.14[11] ^a	-4.71[11] ^a	-5.67[11] ^a	-8.06[10] ^a	3.15[11] ^a	6.30[11] ^a
50	2.15[11]	3.79[12]	4.98[12]	-2.49[12]	-3.00[12]	-4.36[11]	1.66[12]	3.31[12]
	2.15[11] ^a	3.79[12] ^a	4.98[12] ^a	-2.49[12] ^a	-3.00[12] ^a	-4.36[11] ^a	1.66[12] ^a	3.31[12] ^a
				$-2.06 \pm 0.06[12]^b$	$-2.79 \pm 0.10[12]^b$	$-4.36[11]^a$	$1.67 \pm 0.07[12]^b$	$2.67 \pm 0.23[12]^b$
							$2.07 \pm 0.06[12]^c$	$3.77 \pm 0.08[12]^c$
60	8.22[11]	1.46[13]	1.87[13]	-9.36[12]	-1.19[13]	-1.90[12]	6.17[12]	1.30[13]
70	1.91[12]	4.74[13]	5.91[13]	-3.14[13]	-3.61[13]	-5.05[12]	2.10[13]	3.94[13]
	$1.84 \pm 0.02[12]^d$							

at the double magic wavelength $\lambda^{(d)} = 1,064.4350$ nm, which is blue-detuned by $\Delta = 710.84$ MHz from the resonance; here, the detuning Δ is calculated according to $\Delta = c/\lambda^{(d)} - c/\lambda^{(\text{res})}$ ($\lambda^{(\text{res})}$ denotes the resonance wavelength). The second column of Table V contains $\lambda^{(d)}$ for the ground state and the $nS_{1/2,|1/2\rangle}$ Rydberg

series (n is listed in the first column) for the auxiliary state $7P_{3/2,|1/2\rangle}$ [same auxiliary state as considered in Fig. 5(a)]. The third and fourth columns of Table V report Δ and the corresponding polarizability $\alpha_v^{(d)}$.

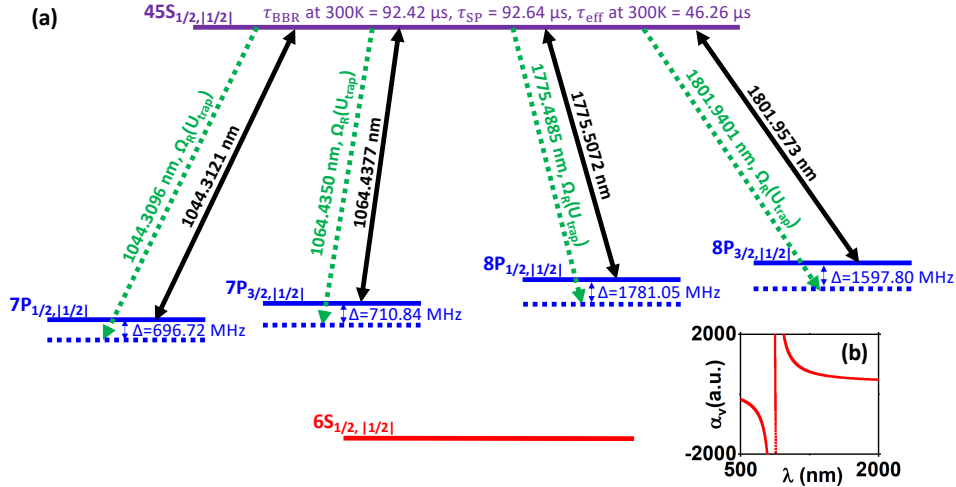


FIG. 4. (a) Schematic energy level diagram of the cesium $6S_{1/2,|1/2\rangle}$ ground state, the $45S_{1/2,|1/2\rangle}$ Rydberg state, and four auxiliary states ($7P_{1/2,|1/2\rangle}$, $7P_{3/2,|1/2\rangle}$, $8P_{1/2,|1/2\rangle}$, and $8P_{3/2,|1/2\rangle}$). The blackbody radiation lifetime τ_{BBR} , spontaneous lifetime τ_{SP} , and effective lifetime τ_{eff} of the $45S_{1/2,|1/2\rangle}$ state in the absence of any trapping light are noted. Black solid and green dotted arrows represent the resonance wavelength $\lambda^{(\text{res})}$ and the magic wavelength $\lambda^{(d)}$ of the trapping light, respectively. The detuning Δ to the auxiliary state is indicated. The Rabi frequency Ω_R for the Rydberg state–auxiliary state transition depends on the trap depth $|U_{\text{trap}}|$ (see discussion in Sec. IV). (b) Dynamic polarizability $\alpha_v(\omega)$ of the ground state as a function of the wavelength λ . The large slope of $\alpha_v(\omega)$ near 870 nm originates in the $6S_{1/2} - 6P_{1/2}$ resonance line at 894.5930 nm and the $6S_{1/2} - 6P_{3/2}$ resonance line at 852.3473 nm.

Figures (not shown) similar to Fig. 5 demonstrate that double magic wavelengths also exist for the other three auxiliary states enumerated in Fig. 4. Figure 6 shows $\lambda^{(d)}$ for the $nS_{1/2,|1/2\rangle}$ series as a function of n ($n \in [40, 70]$)

for the same auxiliary states as those considered in Fig. 4. Two double magic wavelengths lie around 1,050 nm (auxiliary states with $n = 7$ and $L = P$) and two lie around 1,790 nm (auxiliary states with $n = 8$ and $L = P$).

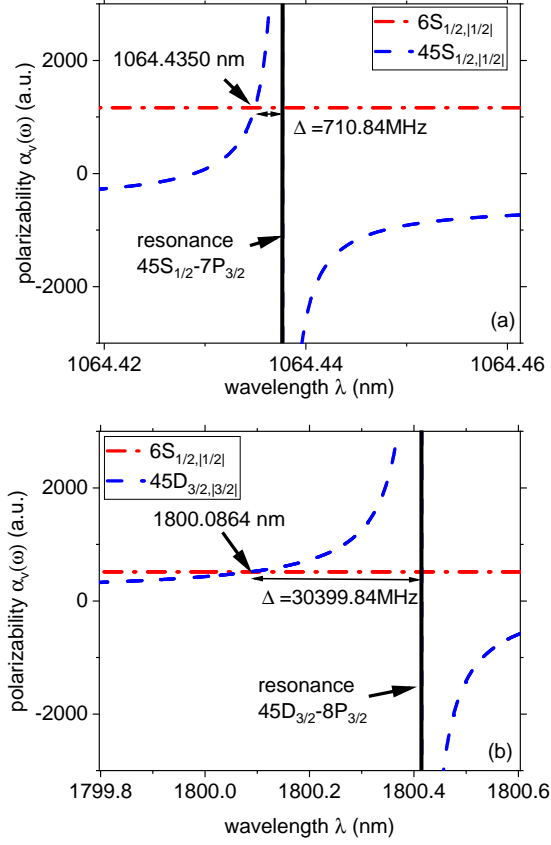


FIG. 5. Dynamic polarizability $\alpha_v(\omega)$ of the $6S_{1/2,|1/2|}$ ground state (red dash-dotted line) and the Rydberg state (blue dashed line) for (a) the $45S_{1/2,|1/2|}$ state with auxiliary state $7P_{3/2,|1/2|}$ and (b) the $45D_{3/2,|3/2|}$ state with auxiliary state $8P_{3/2,|3/2|}$. The intersection of the polarizability curves occurs at the double magic wavelengths (marked by an arrow) of (a) $\lambda^{(d)} = 1,064.4350$ nm and (b) $\lambda^{(d)} = 1,800.0864$ nm. The resonance position is marked by the black solid vertical lines. The detuning of the double magic wavelength from the resonance transition is (a) $\Delta = 710.84$ MHz and (b) $\Delta = 30,399.84$ MHz.

The corresponding detuning Δ from the resonance line is shown in the insets. Figure 6 shows that both the double magic wavelengths and detunings decrease monotonically with increasing n for each of the four auxiliary states considered.

Employing the same format as used in Table V, Tables S.2-S.34 of the supplemental material [44] contain the double magic wavelengths, detunings, and respective polarizabilities for all other Rydberg series considered

IV. INTERPRETATION AND EXPERIMENTAL FEASIBILITY OF DOUBLE MAGIC WAVELENGTH TRAPPING

The polarizability for the ground state and the Rydberg state are equal at $\lambda^{(d)}$ reported in the previous sec-

tion. Typically, one would like to work with large detunings to minimize light scattering [3]. Inspection of Tables V and S.2-S.34 shows that Δ is particularly large (greater than 5,000 MHz for $n = 40$) for the $nD_{3/2,|1/2|}$ series (auxiliary states $7P_{1/2,|1/2|}$, $8P_{1/2,|1/2|}$, and $4F_{5/2,|1/2|}$), the $nD_{3/2,|3/2|}$ series (auxiliary states $7P_{3/2,|3/2|}$, $8P_{3/2,|3/2|}$, and $4F_{5/2,|3/2|}$), the $nD_{5/2,|1/2|}$

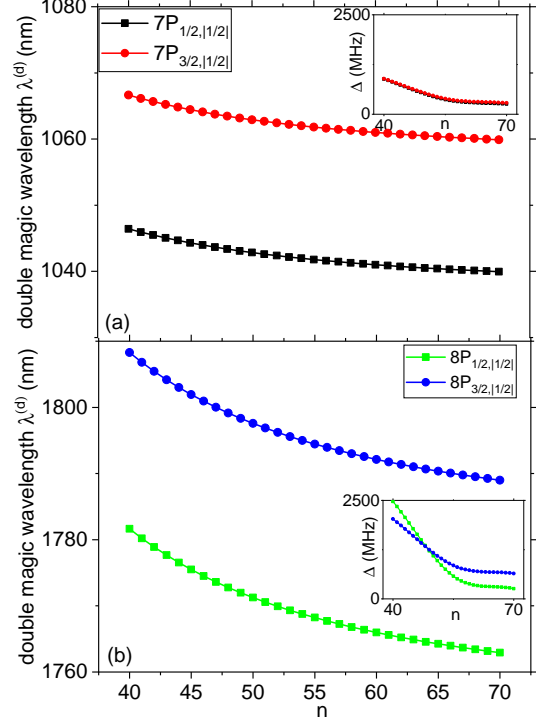


FIG. 6. Double magic wavelength $\lambda^{(d)}$ for the ground state and the $nS_{1/2,|1/2|}$ Rydberg series as a function of n for the auxiliary states (a) $7P_{1/2,|1/2|}$ and $7P_{3/2,|1/2|}$, and (b) $8P_{1/2,|1/2|}$ and $8P_{3/2,|1/2|}$. The insets show the corresponding detuning Δ . In the inset of (a), the detunings for the $7P_{1/2,|1/2|}$ and $7P_{3/2,|1/2|}$ auxiliary states are nearly indistinguishable.

series (auxiliary state $8P_{3/2,|1/2|}$), and the $nD_{5/2,|3/2|}$ series (auxiliary state $8P_{3/2,|3/2|}$). As an example of these larger detuning cases, Fig. 5(b) shows the dynamic polarizability for the $45D_{3/2,|3/2|}$ state near the $45D_{3/2,|3/2|} - 8P_{3/2,|3/2|}$ resonance line; for this case, Δ is equal to 30,399.84 MHz. As discussed in Sec. IV, an assessment of the experimental feasibility of double magic wavelength trapping depends not only on the detuning value but also on the lifetime of the auxiliary state and on the coupling strength between the Rydberg state and the auxiliary state.

tion. For a given light intensity I , the depth $|U_{\text{trap}}|/k_B$ of the trapping potential is proportional to the polar-

TABLE IV. Rydberg states (column 1) and corresponding auxiliary states (columns 2) considered in this work (only auxiliary states that yield double magic wavelengths are listed). Auxiliary states for which triple magic wavelengths exist are in bold. Column 3 lists the lifetime of the auxiliary state. Entries marked by the superscripts a , b , c , d , e , and f are experimental data taken from Ref. [45], Ref. [46], Ref. [47], Ref. [48], Ref. [49], and Ref. [50], respectively. The lifetime of the auxiliary state $7P_{1/2,|1/2|}$, e.g., is 155 ns, with an uncertainty of 4 ns. Column 4 indicates the table number where the double and triple magic wavelengths are reported. For example, the double magic wavelengths $\lambda^{(d)}$ for simultaneous trapping of the ground state and a state from the $nS_{1/2,|1/2|}$ Rydberg series, using the auxiliary state $7P_{3/2,|1/2|}$, can be found in Table V while the triple magic wavelengths $\lambda^{(t)}$ can be found in Table S.35.

Rydberg series	auxiliary state	lifetime (ns)	table number
$nS_{1/2, 1/2 }$	$7P_{1/2, 1/2 }$	155(4) ^a	S.2/—
	$7P_{3/2, 1/2 }$	133(2) ^a	V/S.35
	$8P_{1/2, 1/2 }$	307(14) ^b	S.3/S.36
	$8P_{3/2, 1/2 }$	274(12) ^b	S.4/ VI
$nP_{1/2, 1/2 }$	$6D_{3/2, 1/2 }$	60.0(2.5) ^c	S.5/S.37
	$8S_{1/2, 1/2 }$	87(9) ^d	S.6/S.38
	$7D_{3/2, 1/2 }$	89(1) ^e	S.7/S.39
$nP_{3/2, 1/2 }$	$6D_{3/2, 1/2 }$	60.0(2.5) ^c	S.8/S.40
	$6D_{5/2, 1/2 }$	60.7(2.5) ^c	S.9/S.41
	$8S_{1/2, 1/2 }$	87(9) ^d	S.10/S.42
	$7D_{3/2, 1/2 }$	89(1) ^e	S.11/S.43
	$7D_{5/2, 1/2 }$	89(1) ^e	S.12/S.44
$nP_{3/2, 3/2 }$	$6D_{3/2, 3/2 }$	60.0(2.5) ^c	S.13/S.45
	$6D_{5/2, 3/2 }$	60.7(2.5) ^c	S.14/S.46
	$7D_{3/2, 3/2 }$	89(1) ^e	S.15/S.47
	$7D_{5/2, 3/2 }$	89(1) ^e	S.16/S.48
$nD_{3/2, 1/2 }$	$7P_{1/2, 1/2 }$	155(4) ^a	S.17/—
	$7P_{3/2, 1/2 }$	133(2) ^a	S.18/S.49
	$8P_{1/2, 1/2 }$	307(14) ^b	S.19/S.50
	$8P_{3/2, 1/2 }$	274(12) ^b	S.20/S.51
	$4F_{5/2, 1/2 }$	40(6) ^f	S.21/S.52
$nD_{3/2, 3/2 }$	$7P_{3/2, 3/2 }$	133(2) ^a	S.22/S.53
	$8P_{3/2, 3/2 }$	274(12) ^b	S.23/S.54
	$4F_{5/2, 3/2 }$	40(6) ^f	S.24/S.55
$nD_{5/2, 1/2 }$	$7P_{3/2, 1/2 }$	133(2) ^a	S.25/S.56
	$8P_{3/2, 1/2 }$	274(12) ^b	S.26/S.57
	$4F_{5/2, 1/2 }$	40(6) ^f	S.27/—
	$4F_{7/2, 1/2 }$	40(6) ^f	S.28/—
$nD_{5/2, 3/2 }$	$7P_{3/2, 3/2 }$	133(2) ^a	S.29/S.58
	$8P_{3/2, 3/2 }$	274(12) ^b	S.30/S.59
	$4F_{5/2, 3/2 }$	40(6) ^f	S.31/S.60
	$4F_{7/2, 3/2 }$	40(6) ^f	S.32/S.61
	$4F_{7/2, 5/2 }$	40(6) ^f	S.33/S.62
$nD_{5/2, 5/2 }$	$4F_{5/2, 5/2 }$	40(6) ^f	S.33/S.62
	$4F_{7/2, 5/2 }$	40(6) ^f	S.34/S.63

Shallow traps with depths as small as 1 μ K can be realized experimentally, though reaching sufficiently low temperatures is, admittedly, challenging [51]. We choose

izability, $U_{\text{trap}} = -I\alpha_v(\omega)/(2\epsilon_0 c)$, where k_B denotes the Boltzmann constant and ϵ_0 the vacuum permittivity [32]. Intuition tells us that a magic wavelength for which the value of the corresponding polarizability $\alpha_v^{(d)}$ is large is a better candidate from an experimental perspective than that for which $\alpha_v^{(d)}$ is small. For the double magic wavelengths reported, $\alpha_v^{(d)}$ is between about 500 – 1,300 a.u. (these values are neither particularly large nor particularly small). For a fixed polarizability, $|U_{\text{trap}}|/k_B$ can be increased by increasing I . Unfortunately, though, there is a penalty associated with cranking up I as this not only increases $|U_{\text{trap}}|/k_B$ but also enhances the coupling to the auxiliary state [36].

Recall that the laser wavelength is, for the Rydberg state, blue-detuned (positive detuning) relative to the auxiliary state. If the detuning Δ from the auxiliary state is very small, it inevitably leads to a mixing of the states, namely of the Rydberg state and the auxiliary state, resulting in potentially significant photon scattering during the trapping process [32]. The larger I , the stronger the mixing of the states. In experiment, one aims to minimize the mixing of the states by choosing I such that the Rabi frequency Ω_R for the transition between the Rydberg state and the auxiliary state is much smaller than the corresponding Δ . Within a two-state model [32], the Rabi frequency Ω_R and the maximal transition probability P_{max} from the Rydberg state ψ_i to the auxiliary state ψ_k are given by

$$\Omega_R = \sqrt{I} |\langle \psi_k | |d| | \psi_i \rangle| \quad (4.1)$$

and

$$P_{\text{max}} = \frac{|\Omega_R|^2}{|\Omega_R|^2 + \Delta^2}, \quad (4.2)$$

respectively.

Figure 7 presents the dependence of P_{max} on n for the nine Rydberg series considered in this paper; as before, all the auxiliary states listed in Table IV are investigated. The corresponding Rabi frequencies are shown in the insets. Tables V and S.2-S.34 report Ω_R , P_{max} , and I for simultaneously trapping the ground state and a Rydberg state. The calculations are performed for a trap depth of $|U_{\text{trap}}|/k_B = 1 \mu\text{K}$. As expected, for a fixed trap depth, Ω_R decreases monotonically with increasing n . Even though Ω_R and Δ (see the insets of Fig. 6) decrease monotonically with n , P_{max} displays a non-monotonic variation with n due to the non-monotonic variation of the derivative of Δ with increasing n .

1 μ K as a reference point, since the dipole force F_{dipole} for this trap depth is still significantly larger than the magnitude of the gravitational force mg , where m de-

TABLE V. Double magic wavelength $\lambda^{(d)}$ for the $6S_{1/2,|1/2\rangle}$ ground state and the $nS_{1/2,|1/2\rangle}$ Rydberg series for $n = 40 - 70$. In all cases, $\lambda^{(d)}$ is blue-detuned (positive Δ) from the auxiliary state $7P_{3/2,|1/2\rangle}$. The polarizability at the magic wavelength is $\alpha_v^{(d)}$. For a trap depth of $|U_{\text{trap}}|/k_B = 1 \mu\text{K}$, the light intensity I , the Rabi frequency Ω_R for the transition between the Rydberg state and the auxiliary state, and the associated maximal transition probability P_{max} (see text) are presented. Following the same format as employed in this table, Tables S.2-S.34 of the supplemental material [44] consider the other Rydberg series and auxiliary states considered in this work.

state	auxiliary state $7P_{3/2, 1/2\rangle}$					
	$\lambda^{(d)}$ (nm)	Δ (MHz)	$\alpha_v^{(d)}$ (a.u.)	I (Wcm^{-2})	Ω_R (MHz)	P_{max}
$40S_{1/2, 1/2\rangle}$	1066.6447	892.33	1152.4154	386.01	205.58	0.050
$41S_{1/2, 1/2\rangle}$	1066.1293	858.13	1154.6188	385.27	196.94	0.050
$42S_{1/2, 1/2\rangle}$	1065.6545	822.53	1156.6592	384.59	188.91	0.050
$43S_{1/2, 1/2\rangle}$	1065.2162	785.89	1158.5519	383.96	181.41	0.051
$44S_{1/2, 1/2\rangle}$	1064.8108	748.54	1160.3102	383.38	174.40	0.051
$45S_{1/2, 1/2\rangle}$	1064.4350	710.84	1161.9475	382.84	167.84	0.053
$46S_{1/2, 1/2\rangle}$	1064.0860	673.14	1163.4732	382.34	161.68	0.055
$47S_{1/2, 1/2\rangle}$	1063.7613	635.79	1164.8982	381.87	156.02	0.057
$48S_{1/2, 1/2\rangle}$	1063.4586	599.15	1166.2306	381.43	150.45	0.059
$49S_{1/2, 1/2\rangle}$	1063.1762	563.55	1167.4782	381.03	145.31	0.062
$50S_{1/2, 1/2\rangle}$	1062.9121	529.35	1168.6479	380.65	140.47	0.066
$51S_{1/2, 1/2\rangle}$	1062.6648	496.90	1169.7463	380.29	135.89	0.070
$52S_{1/2, 1/2\rangle}$	1062.4329	466.55	1170.7788	379.95	131.56	0.074
$53S_{1/2, 1/2\rangle}$	1062.2152	438.66	1171.7506	379.64	127.45	0.078
$54S_{1/2, 1/2\rangle}$	1062.0105	413.56	1172.6664	379.34	123.56	0.082
$55S_{1/2, 1/2\rangle}$	1061.8178	391.61	1173.5301	379.06	119.86	0.086
$56S_{1/2, 1/2\rangle}$	1061.6362	373.04	1174.3461	378.80	116.34	0.089
$57S_{1/2, 1/2\rangle}$	1061.4648	357.63	1175.1176	378.55	112.99	0.091
$58S_{1/2, 1/2\rangle}$	1061.3029	345.02	1175.8474	378.31	109.80	0.092
$59S_{1/2, 1/2\rangle}$	1061.1498	334.85	1176.5390	378.09	106.76	0.092
$60S_{1/2, 1/2\rangle}$	1061.0049	326.79	1177.1947	377.88	103.86	0.092
$61S_{1/2, 1/2\rangle}$	1060.8676	320.47	1177.8167	377.68	101.09	0.091
$62S_{1/2, 1/2\rangle}$	1060.7373	315.56	1178.4080	377.49	98.44	0.089
$63S_{1/2, 1/2\rangle}$	1060.6137	311.69	1178.9695	377.31	95.91	0.086
$64S_{1/2, 1/2\rangle}$	1060.4962	308.53	1179.5044	377.14	93.48	0.084
$65S_{1/2, 1/2\rangle}$	1060.3845	305.71	1180.0132	376.98	91.15	0.082
$66S_{1/2, 1/2\rangle}$	1060.2781	302.90	1180.4984	376.82	88.92	0.079
$67S_{1/2, 1/2\rangle}$	1060.1768	299.73	1180.9608	376.68	86.78	0.077
$68S_{1/2, 1/2\rangle}$	1060.0803	295.87	1181.4020	376.54	84.72	0.076
$69S_{1/2, 1/2\rangle}$	1059.9882	290.95	1181.8237	376.40	82.75	0.075
$70S_{1/2, 1/2\rangle}$	1059.9002	284.64	1182.2263	376.27	80.85	0.075

notes the mass of the ^{133}Cs atom and g the gravitational acceleration. To estimate F_{dipole} , we consider a one-dimensional harmonic potential with angular frequency ω_{HO} along the z -coordinate that changes to a constant for $|z|$ larger than the waist z_R of the dipole trap beam. Evaluating the force at z_R and setting $\omega_{\text{HO}} = \sqrt{2|U_{\text{trap}}|/(mz_R^2)}$, we find $F_{\text{dipole}} = -2U_{\text{trap}}/z_R$. To give a concrete example, a beam waist of $0.5 \mu\text{m}$ corresponds to $\omega_{\text{HO}} = 2\pi \times 3.56 \text{ kHz}$ for $|U_{\text{trap}}|/k_B = 1 \mu\text{K}$. Expressing z_R as $\gamma/\sqrt{2m|U_{\text{trap}}|}$, where γ is a dimensionless scaling factor that is—for physical reasons—constrained to $\gamma \gtrsim 1$ (if γ was smaller than 1 the ground state wave function would not fit into the trap), we have $F_{\text{dipole}} = \gamma^{-1}\sqrt{m}(2|U_{\text{trap}}|)^{3/2}$ (recall, \hbar has been set to 1). Figure 8 compares the dipole force and the gravitational force for cesium as a function of $|U_{\text{trap}}|/k_B$. In plotting the dipole force, we set $\gamma = 1$, i.e., we assumed the “best case scenario”. If one wanted to trap multiple motional states, γ would need to be larger than one, im-

plying that F_{dipole} would be smaller. It can be seen that the dipole force for a trap depth of $1 \mu\text{K}$ is three orders of magnitude larger than the gravitational force. Figure 8 thus suggests that one may even be able to achieve trapping for trap depths a bit shallower than $1 \mu\text{K}$. We note that the use of a more realistic functional form for the dipole trap potential yields to a dipole force that is four times smaller than the harmonic oscillator potential based estimate presented here. While the detailed functional form of the trap, including the confinement along the x - and y -directions, needs to be taken into account when analyzing a specific experimental set-up, the analysis presented in this paper should serve as a useful reference point.

Figure 7 as well as Tables V and S.2-S.34 show that P_{max} , calculated for $|U_{\text{trap}}|/k_B = 1 \mu\text{K}$, varies greatly for the Rydberg series, auxiliary states, and principal quantum numbers considered. The smallest P_{max} values are found for:

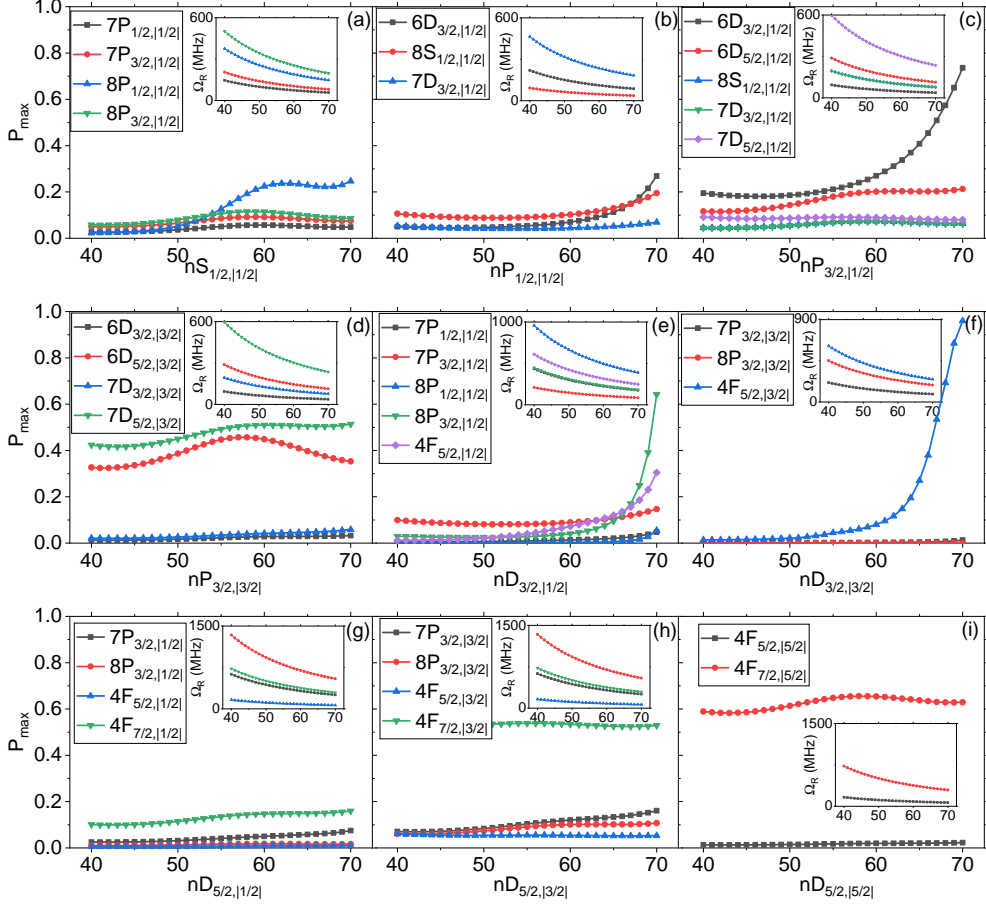


FIG. 7. Maximal transition probability P_{\max} , i.e., maximal probability that the Rydberg state transitions to the auxiliary state, for $|U_{\text{trap}}|/k_B = 1 \mu\text{K}$ as a function of the principal quantum number n ; P_{\max} is estimated using a two-state model (see text for details). The insets show the corresponding Rabi frequency Ω_R . Each panel corresponds to a different Rydberg series (see the x -axis). The auxiliary states considered are shown in the legend in each panel. The values of P_{\max} and respective magic wavelengths, detunings, and polarizabilities are tabulated in Table V and Tables S.2-S.34 of the supplemental material [44].

- $nD_{3/2,1/2}$ series with auxiliary state $7P_{1/2,1/2}$,
- $nD_{3/2,1/2}$ series with auxiliary state $8P_{1/2,1/2}$,
- $nD_{3/2,3/2}$ series with auxiliary state $7P_{3/2,3/2}$,
- $nD_{3/2,3/2}$ series with auxiliary state $8P_{3/2,3/2}$,
and
- $nD_{5/2,1/2}$ series with auxiliary state $4F_{5/2,1/2}$.

Considering that the trapping of a Rydberg state does not only require a sufficiently small P_{\max} but also a sufficiently long lifetime of the auxiliary state (the lifetimes are listed in Table IV), the $nD_{3/2,1/2}$ series with auxiliary state $8P_{1/2,1/2}$ [lifetime of 307(14) ns] and the $nD_{3/2,3/2}$ series with auxiliary state $8P_{3/2,3/2}$ [lifetime of 274(12) ns] are the most promising. To estimate realistic trapping times, we solve a 12-state (13-state) master equation for the $45D_{3/2,1/2}$ ($45D_{3/2,3/2}$) cases [52]. Working in the rotating frame within the rotating wave

approximation, the coupling matrix element for the Rydberg state, which is detuned by Δ and assumed to be infinitely long-lived, and the auxiliary state is given by $-\Omega_R/2$. The spontaneous lifetimes of the auxiliary state and the low-lying excited states that the auxiliary state can decay into, either directly or through intermediate states such as $6P_{1/2}$, $6P_{3/2}$, etc., is treated through dissipators that depend on Lindbladian operators.

The black, red, and blue lines in Fig. 9 show the population $|c_{\text{Ryd}}|^2$ of the Rydberg state as a function of time for $|U_{\text{trap}}|/k_B = 1, 10,$ and $100 \mu\text{K}$, respectively. Figure 9(a) considers the $45D_{3/2,1/2}$ state while Fig. 9(b) considers the $45D_{3/2,3/2}$ state. At $t = 0$, the system is initialized in the Rydberg state. At short times (see the insets in Fig. 9), the population oscillates rapidly at a time scale that is set by the effective Rabi coupling strength. The oscillations are damped at longer times by the incoherent decay processes. Figure 9(a) shows that the probability to be in the Rydberg state after $5 \mu\text{s}$ is around 53.4, 93.3, and 99.3 % for the $45D_{3/2,1/2}$ state

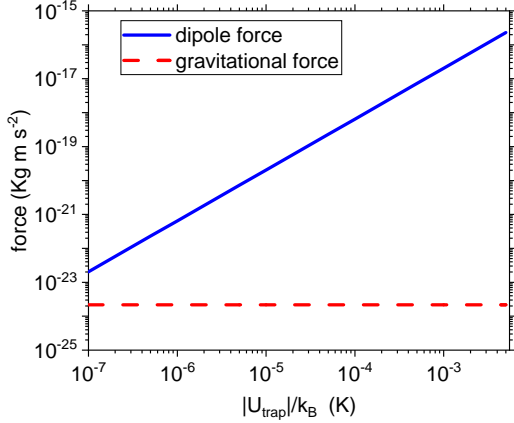


FIG. 8. Dipole and gravitational force for a cesium atom as a function of the trap depth $|U_{\text{trap}}|/k_B$ (note the log-log scale). The dipole force (blue solid line) is significantly larger than the gravitational force (red dashed line) for traps as shallow as $0.1 \mu\text{K}$.

for trap depths of 100, 10, and $1 \mu\text{K}$, respectively. For the $45D_{3/2,|3/2\rangle}$ state, in contrast, the probability to be in the Rydberg state after $5 \mu\text{s}$ is 92.8, 99.2, and 99.9 % for the same trap depths. The probability $|c_{\text{Ryd}}|^2$ may, depending on the Rydberg series, vary notably with n . For the $nD_{3/2,|1/2\rangle}$ series ($8P_{1/2,|1/2\rangle}$ auxiliary state), e.g., $|c_{\text{Ryd}}|^2$ at $t = 5 \mu\text{s}$ is larger than 0.99 for $n = 40 - 57$ and then decreases to 0.777 for $n = 70$ for a trap depth of $1 \mu\text{K}$. For the $nD_{3/2,|3/2\rangle}$ series ($8P_{3/2,|3/2\rangle}$ auxiliary state), in contrast, $|c_{\text{Ryd}}|^2$ at $t = 5 \mu\text{s}$ increases from 0.9990 for $n = 40$ to 0.9997 for $n = 70$ (these numbers are, again, for a trap depth of $1 \mu\text{K}$). Our master equation simulations demonstrate that the proposed trapping scheme is feasible, opening the door for Rydberg state-based simulations on time scales up to tens of microseconds.

Our discussion up to now assumed that the atomic energy levels and states are labeled by the quantum numbers n , L , J , and the magnitude of M_J , i.e., we assumed that hyperfine state splittings are not resolved. Typical cold atom experiments are, however, sensitive to hyperfine splittings, dictating that one should consider that the total electron angular momentum (labeled by J) and the nuclear spin (labeled by I_N) combine to the total angular momentum (labeled by F with associated projection quantum number M_F). For ^{133}Cs with $I_N = 7/2$, there exist two ground state manifolds ($F = 3$ and 4) that contain a total of 16 states. Since the scalar polarizability is unchanged when changing from the (J, M_J, I_N, M_I) to the (J, I_N, F, M_F) basis, all the $F = 3$ and 4 ground states have the same polarizability as the $6S_{1/2,|1/2\rangle}$ state (the tensor polarizability does not enter). For the Rydberg states with $J = 1/2$, the same argument applies. For Rydberg states with $J = 3/2$ and $5/2$, in contrast, the tensor polarizability, which changes under the change of basis, enters. Appendix C shows that the result-

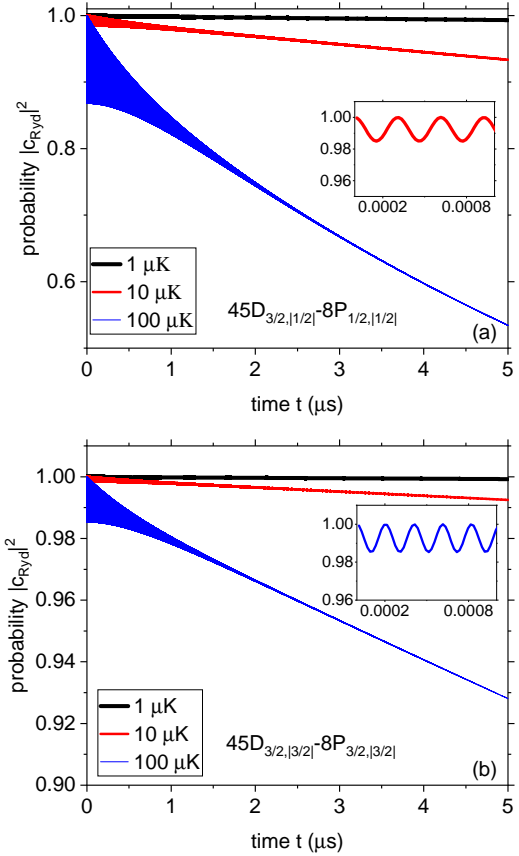


FIG. 9. Probability $|c_{\text{Ryd}}|^2$ to be in the Rydberg state, determined by solving a master equation, for trap depths $|U_{\text{trap}}|/k_B = 1 \mu\text{K}$ (black line; top line at $t = 1 \mu\text{s}$), $10 \mu\text{K}$ (red line; middle line at $t = 1 \mu\text{s}$), and $100 \mu\text{K}$ (blue line; bottom line at $t = 1 \mu\text{s}$). (a) and (b) consider the Rydberg state $45D_{3/2,|1/2\rangle}$ with auxiliary state $8P_{1/2,|1/2\rangle}$ and the Rydberg state $45D_{3/2,|3/2\rangle}$ with auxiliary state $8P_{3/2,|3/2\rangle}$, respectively. Notes the different y scales in (a) and (b). The insets show an enlargement of the short-time region for (a) the $10 \mu\text{K}$ trap and (b) the $100 \mu\text{K}$ trap.

ing change of the magic wavelengths is of the order of 0.01 nm . Since there is an uncertainty in the magic wavelength determination anyways due to approximations made in the matrix element determination, etc., the magic wavelengths predicted using the (J, M_J, I_N, M_I) basis provide a faithful starting point for precisely pinpointing magic wavelength conditions experimentally.

V. MULTI-MAGIC CONDITIONS: TRIPLE AND QUADRUPLE MAGIC WAVELENGTHS

This section shows that there exist wavelengths that lead to trapping of not only the ground state and a Rydberg state but also of low-lying excited states. Specifically, it is shown that there exist conditions for which

the $6P_{3/2,|M_J|}$ state [radiative lifetime of 30.0(7) ns], the $5D_{3/2,|M_J|}$ state [radiative lifetime of 966(34) ns], or the $5D_{5/2,|M_J|}$ state [radiative lifetime of 1,353(5) ns] are trapped along with the ground state and a Rydberg state; the associated wavelengths are referred to as triple magic wavelengths $\lambda^{(t)}$. In addition, we identify seven quadruple magic wavelengths $\lambda^{(q)}$ at which four states (including the ground state and a Rydberg state) are trapped simultaneously (tens of approximate quadrupole magic wavelengths are also identified). We refer to the low-lying excited states as intermediate states.

We do not find any multi-magic wavelengths in the range 1,000 – 2,000 nm for the Rydberg series $nS_{1/2}$, $nP_{1/2}$, $nP_{3/2}$, $nD_{3/2}$, and $nD_{5/2}$ with $n = 40 - 70$ if the quantization axis, set by \vec{B}_{ext} , and the polarization vector are parallel [$\theta = 0$; see Fig. 2(a)]. If, however, the angle θ between the quantization axis and the polarization vector, which enters through the prefactor $(3 \cos^2 \theta - 1)/2$ into the dynamic tensor polarizability [see Fig. 2(b) and Eq. (B3)], is varied, we find—as discussed below—many multi-magic wavelengths. For what follows, it is important to keep in mind that the polarizability of states with $J = 1/2$ does not depend on θ for linearly polarized Gaussian light. Moreover, the polarizability of the Rydberg states considered is essentially independent of θ for the n values considered in this work. Thus, we aim to adjust the polarizability of candidate intermediate states that have $J > 1/2$ by tuning θ .

To illustrate the tunability afforded by θ , Fig. 10 shows the dynamic polarizability of the ground state $6S_{1/2,|1/2|}$ (red dashed curve) and two low-lying excited states, namely $5D_{5/2,|5/2|}$ (purple lines) and $6P_{3/2,|1/2|}$ (blue lines), for $\cos^2 \theta = 0, 1/3$, and 1. These angles correspond to $(3 \cos^2 \theta - 1)/2 = -1/2, 0$, and 1, respectively. Interestingly, we find that the magic wavelength for the ground state and the state $5D_{5/2,|5/2|}$ near the $5D_{5/2} - 7P_{3/2}$ resonance line decreases with increasing $\cos^2 \theta$ while that for the ground state and the state $6P_{3/2,|1/2|}$ near the $6P_{3/2} - 7S_{1/2}$ resonance line increases with increasing $\cos^2 \theta$. It can be seen that changes in θ lead to magic wavelength shifts as large as 300 nm. This tunability of the dynamic polarizabilities of the low-lying states through the angle θ is leveraged in the discussion that follows.

Figure 11 displays triple magic conditions for four Rydberg series, namely (a) the $nS_{1/2,|1/2|}$ series (auxiliary state $8P_{3/2,|1/2|}$), (b) the $nP_{3/2,|1/2|}$ series (auxiliary state $7D_{3/2,|1/2|}$), (c) the $nD_{3/2,|1/2|}$ series (auxiliary state $8P_{1/2,|1/2|}$), and (d) the $nD_{5/2,|1/2|}$ series (auxiliary state $8P_{3/2,|1/2|}$). To explain the plots, let us first focus on Fig. 11(a). The x -axis shows the previously identified $\lambda^{(d)}$ for simultaneous trapping of the ground state and the $nS_{1/2,|1/2|}$ Rydberg state (even though the double magic wavelengths were previously discussed for $\theta = 0$, these double magic wavelengths are, as noted in the pre-

vious paragraph, independent of θ). The top axis indicates the n value: the state with $n = 70$ corresponds to the smallest double magic wavelength and that with

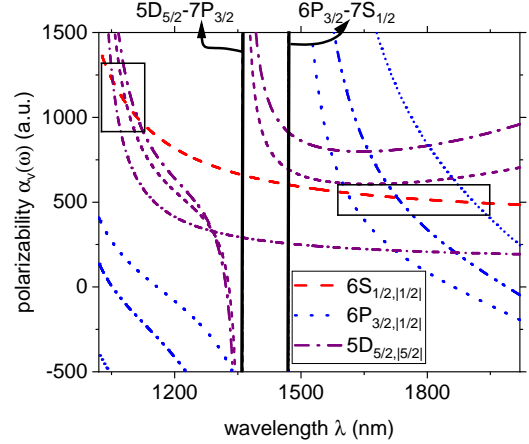


FIG. 10. Dynamic polarizability $\alpha_v(\omega)$ of the ground state $6S_{1/2,|1/2|}$ and two low-lying excited states, namely $5D_{5/2,|5/2|}$ and $6P_{3/2,|1/2|}$, for three different angles θ between the quantization axis and the polarization vector for linearly polarized Gaussian light. The vertical black solid lines indicate the resonance lines. The red dashed line shows the polarizability of the $6S_{1/2,|1/2|}$ state. The purple long-dash-dotted, dashed, and short-dash-dotted lines show the polarizability for the $5D_{5/2,|5/2|}$ state for $\cos^2 \theta = 0, 1/3$, and 1, respectively. Similarly, blue wide-spaced-dotted, dash-dot-dotted, and dotted lines show the polarizability for the $6P_{3/2,|1/2|}$ state for $\cos^2 \theta = 0, 1/3$, and 1, respectively. The black boxes draw the reader’s attention to how the magic wavelength between the ground state and the low-lying excited state varies when θ is changed.

$n = 40$ to the largest double magic wavelength. The blue up-triangles show the value of $\cos^2 \theta$ for which the intermediate state $5D_{3/2,|3/2|}$ is trapped, i.e., the double magic wavelength becomes triple magic for this specific angle θ . For the $nS_{1/2,|1/2|}$ series with auxiliary state $8P_{3/2,|1/2|}$, five intermediate states are identified that have triple magic wavelengths for specific θ for all n considered. Table VI summarizes the triple magic wavelengths $\lambda^{(t)}$ as a function of n for the auxiliary state $8P_{3/2,|1/2|}$. Tables S.35-S.63 show analogous results for different auxiliary states and different Rydberg series.

Interestingly, the curves for the $6P_{3/2,|3/2|}$ and $5D_{5/2,|1/2|}$ states in Fig. 11(a) cross at $n \approx 53$, signaling the existence of a quadruple magic wavelength $\lambda^{(q)}$. Similarly, Fig. 11(c) indicates the existence of a quadruple magic wavelength that leads to trapping of the states $6S_{1/2,|1/2|}$, $42D_{3/2,|1/2|}$, $6P_{3/2,|1/2|}$, and $5D_{5/2,|5/2|}$, and Fig. 11(d) indicates the existence of a quadruple magic wavelength $\lambda^{(q)}$ that leads to trapping of the states $6S_{1/2,|1/2|}$, $54D_{5/2,|1/2|}$, $6P_{3/2,|3/2|}$, and $5D_{5/2,|1/2|}$. Table VII enumerates all $\lambda^{(q)}$ identified in this work, along with the corresponding detunings and polarizabilities.

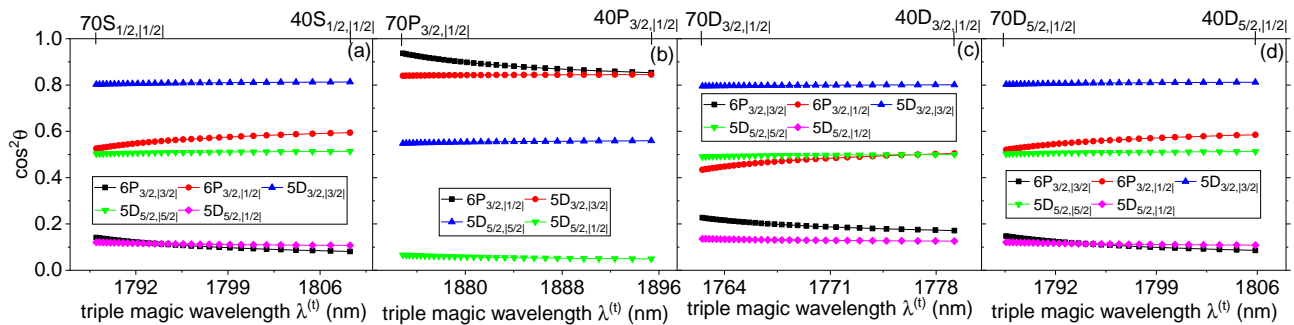


FIG. 11. Triple magic conditions for the ground state, a Rydberg state, and an intermediate state. The value of $\cos^2 \theta$ for which the polarizability of the intermediate state coincides with the polarizability $\alpha_v^{(d)}$ for which the ground state and the Rydberg state are double magic, as a function of the triple magic wavelength $\lambda^{(t)}$ (adjusting θ turns the double magic wavelength into a triple magic wavelength). Each panel considers multiple intermediate states (see legend). The Rydberg states are (a) $nS_{1/2,|1/2|}$ with auxiliary state $8P_{3/2,|1/2|}$, (b) $nP_{3/2,|1/2|}$ with auxiliary state $7D_{3/2,|1/2|}$, (c) $nD_{3/2,|1/2|}$ with auxiliary state $8P_{1/2,|1/2|}$, and (d) $nD_{5/2,|1/2|}$ with auxiliary state $8P_{3/2,|1/2|}$.

Experimentally, one may also be able to use "approximate" quadruple magic wavelengths for which the difference between the θ values for the two intermediate states is rather small, say less than 1.5° (this value is somewhat arbitrary—for some applications, a less stringent criterium might suffice). One such ex-

ample is shown in Fig. 11(b) for the states $6S_{1/2,|1/2|}$, $40P_{3/2,|1/2|}$, $6P_{3/2,|1/2|}$, and $5D_{3/2,|3/2|}$. Tables S.64-S.65 of the supplemental material enumerate all the approximate quadruple magic wavelengths for which the difference between the θ values obtained for two intermediate states is less than 1.5° .

Since ultracold atom experiments are sensitive to the hyperfine structure, it is important to check how a change of the basis from (I_N, M_I, J, M_J) to (J, I_N, F, M_F) impacts the triple magic wavelength conditions. As discussed earlier, the ground state is unaffected by the basis change while the Rydberg state is weakly affected. The low-lying excited states, in contrast, are comparatively strongly affected by the basis change, leading to shifts of the polarizability curves as well as changes of the functional form. Appendix C illustrates, by showing examples, that triple magic wavelengths also exist when accounting for the hyperfine structure. As such, the triple magic wavelength tables provided in this paper serve as a guide for the analysis that accounts for the hyperfine states.

VI. CONCLUSION

This paper presented the lifetime and dynamic polarizability for a ^{133}Cs atom in the Rydberg state with principal quantum number $40 \leq n \leq 70$. Explicitly, we considered all possible total angular momenta J for the Rydberg series nS , nP , and nD . We observed that, in

general, the room temperature ($T = 300$ K) blackbody radiation decay impacts the lifetime of a Rydberg state significantly. The effective lifetime, which is a combination of the spontaneous and blackbody radiation lifetimes, does not scale as n^3 but with a lower power of n , namely the scaling law for the states considered in this work is n^a with $2.3 \leq a \leq 2.69$, where the value of a depends on the orbital angular momentum and total electronic angular momentum of the Rydberg state.

Moreover, we presented static and dynamic polarizabilities for cesium Rydberg states for a linearly polarized Gaussian shaped laser beam, whose polarization vector is parallel to the quantization axis set by the external magnetic field vector \vec{B}_{ext} . The polarizabilities were calculated using the sum-over-state approach and our static scalar and tensor polarizabilities agree well with available theoretical and experimental results.

To confine the ground state and a Rydberg state simultaneously in the same potential well, we utilize a double magic wavelength based trapping scheme for which the wavelength of the laser is blue-detuned for the Rydberg state and red detuned for the ground state. A total of 34 sequences were identified (9 different Rydberg series and a varying number of auxiliary states for each Rydberg

TABLE VI. Values of $\cos^2 \theta$ for which triple magic conditions are fulfilled for the $6S_{1/2,|1/2\rangle}$ ground state, the $nS_{1/2,|1/2\rangle}$ Rydberg state ($n = 40 - 70$), and several intermediate states; see Fig. 2(b) and Eq. (B3) for the definition of θ . The last three columns report the triple magic wavelength $\lambda^{(t)}$, the detuning Δ between the triple magic wavelength and the Rydberg state–auxiliary state transition line, and the associated triple magic polarizability $\alpha_v^{(t)}$. The auxiliary state is $8P_{3/2,|1/2\rangle}$. Following the same format as employed in this table, Tables S.35-S.63 of the supplemental material [44] consider the other Rydberg series and auxiliary states considered in this work.

Rydberg state	$\cos^2 \theta$ for $6P_{3/2, 3/2\rangle}$	$\cos^2 \theta$ for $6P_{3/2, 1/2\rangle}$	$\cos^2 \theta$ for $5D_{3/2, 3/2\rangle}$	$\cos^2 \theta$ for $5D_{5/2, 5/2\rangle}$	$\cos^2 \theta$ for $5D_{5/2, 1/2\rangle}$	$\lambda^{(t)}$ (nm)	Δ (MHz)	$\alpha_v^{(t)}$ (a.u.)
$40S_{1/2, 1/2\rangle}$	0.0814	0.5942	0.8131	0.5136	0.1073	1808.2790	2027.01	512.7849
$41S_{1/2, 1/2\rangle}$	0.0834	0.5919	0.8128	0.5133	0.1077	1806.7987	1946.37	513.0281
$42S_{1/2, 1/2\rangle}$	0.0854	0.5896	0.8124	0.5129	0.1082	1805.4361	1862.27	513.2527
$43S_{1/2, 1/2\rangle}$	0.0873	0.5873	0.8120	0.5126	0.1086	1804.1790	1775.56	513.4605
$44S_{1/2, 1/2\rangle}$	0.0893	0.5850	0.8117	0.5122	0.1091	1803.0168	1687.11	513.6532
$45S_{1/2, 1/2\rangle}$	0.0913	0.5828	0.8113	0.5119	0.1095	1801.9401	1597.80	513.8322
$46S_{1/2, 1/2\rangle}$	0.0933	0.5805	0.8110	0.5115	0.1100	1800.9407	1508.48	513.9988
$47S_{1/2, 1/2\rangle}$	0.0953	0.5782	0.8106	0.5112	0.1105	1800.0113	1420.04	514.1540
$48S_{1/2, 1/2\rangle}$	0.0973	0.5759	0.8103	0.5108	0.1109	1799.1455	1333.33	514.2989
$49S_{1/2, 1/2\rangle}$	0.0993	0.5736	0.8099	0.5105	0.1114	1798.3377	1249.22	514.4344
$50S_{1/2, 1/2\rangle}$	0.1013	0.5713	0.8096	0.5101	0.1118	1797.5828	1168.59	514.5612
$51S_{1/2, 1/2\rangle}$	0.1033	0.5690	0.8092	0.5098	0.1123	1796.8761	1092.29	514.6801
$52S_{1/2, 1/2\rangle}$	0.1053	0.5667	0.8089	0.5094	0.1128	1796.2137	1021.20	514.7918
$53S_{1/2, 1/2\rangle}$	0.1073	0.5644	0.8085	0.5091	0.1132	1795.5919	956.19	514.8968
$54S_{1/2, 1/2\rangle}$	0.1093	0.5622	0.8082	0.5088	0.1137	1795.0074	898.13	514.9956
$55S_{1/2, 1/2\rangle}$	0.1113	0.5599	0.8078	0.5084	0.1141	1794.4573	847.87	515.0887
$56S_{1/2, 1/2\rangle}$	0.1133	0.5576	0.8075	0.5081	0.1146	1793.9388	806.01	515.1766
$57S_{1/2, 1/2\rangle}$	0.1150	0.5553	0.8071	0.5077	0.1150	1793.4498	771.96	515.2596
$58S_{1/2, 1/2\rangle}$	0.1173	0.5530	0.8067	0.5074	0.1155	1792.9878	744.85	515.3381
$59S_{1/2, 1/2\rangle}$	0.1192	0.5507	0.8064	0.5070	0.1160	1792.5510	723.81	515.4124
$60S_{1/2, 1/2\rangle}$	0.1212	0.5484	0.8060	0.5067	0.1164	1792.1376	707.99	515.4827
$61S_{1/2, 1/2\rangle}$	0.1232	0.5461	0.8057	0.5063	0.1169	1791.7459	696.50	515.5495
$62S_{1/2, 1/2\rangle}$	0.1252	0.5439	0.8053	0.5060	0.1173	1791.3744	688.49	515.6129
$63S_{1/2, 1/2\rangle}$	0.1272	0.5416	0.8050	0.5056	0.1178	1791.0218	683.08	515.6730
$64S_{1/2, 1/2\rangle}$	0.1292	0.5393	0.8046	0.5053	0.1183	1790.6868	679.41	515.7303
$65S_{1/2, 1/2\rangle}$	0.1312	0.5370	0.8043	0.5049	0.1187	1790.3682	676.60	515.7847
$66S_{1/2, 1/2\rangle}$	0.1332	0.5347	0.8039	0.5046	0.1192	1790.0651	673.80	515.8366
$67S_{1/2, 1/2\rangle}$	0.1352	0.5324	0.8036	0.5042	0.1196	1789.7764	670.13	515.8860
$68S_{1/2, 1/2\rangle}$	0.1372	0.5301	0.8032	0.5039	0.1201	1789.5013	664.72	515.9332
$69S_{1/2, 1/2\rangle}$	0.1392	0.5278	0.8029	0.5036	0.1205	1789.2388	656.70	515.9782
$70S_{1/2, 1/2\rangle}$	0.1412	0.5255	0.8025	0.5032	0.1210	1788.9884	645.22	516.0211

series), for which the differential ac-Stark shift between the ground state and the Rydberg state is zero. For all the Rydberg series and respective auxiliary states considered, with the exception of the Rydberg series $nP_{3/2,|1/2\rangle}$ with auxiliary state $6D_{3/2,|1/2\rangle}$, the detunings are notably larger than 50 MHz. The Rydberg series $nD_{3/2,|1/2\rangle}$ with auxiliary state $8P_{1/2,|1/2\rangle}$ and $nD_{3/2,|3/2\rangle}$ with auxiliary state $8P_{3/2,|3/2\rangle}$ were found to have particularly large detunings up to 20,000 – 30,000 MHz.

To further assess the applicability of the double magic wavelengths presented, we determined the Rabi frequency and discussed the resulting maximal population transfer from the Rydberg state to the auxiliary state. While the reported P_{\max} are based on a trap depth of 1 μK , the tables contain all the information needed to perform an analogous analysis for other trap depths. We demonstrated, using a master equation formalism that accounts for the spontaneous lifetime of low-lying excited states and the auxiliary state, that an atom in the

$nD_{3/2,|1/2\rangle}$ or $nD_{3/2,|3/2\rangle}$ states can be trapped up to several μs without significant losses, provided the trap is sufficiently shallow. For the nD series, very encouraging results were found for trap depth as large as 10 – 100 μK .

While only a subset of Rydberg and auxiliary states investigated promise to be suitable for long-time trapping, our work suggests other interesting applications. For example, the formalism developed can be used to determine tune-out wavelengths [53, 54], for which the atom in the Rydberg state does neither feel an attractive nor a repulsive force. Operating at tune-out wavelengths might be viewed as a compromise, where the unwanted losses are reduced at the expense of losing the trapping benefits.

Lastly, by tuning the angle θ between the quantization axis and the polarization vector, we found triple magic wavelengths for the ground state, a Rydberg state, and a low-lying excited state as well as several quadruple magic wavelengths for the ground state, a Rydberg state, and two low-lying excited states. The triple magic wavelength

TABLE VII. Values of $\cos^2 \theta$ for which quadruple magic conditions are fulfilled for the $6S_{1/2,|1/2|}$ ground state, a Rydberg state, and two intermediate states (denoted as intermediate state-1 and intermediate state-2) for three different auxiliary states; see Fig. 2(b) and Eq. (B3) for the definition of θ . A total of seven quadruple magic conditions were found. The last three columns report the quadruple magic wavelength $\lambda^{(q)}$, the detuning Δ between the quadruple magic wavelength and the Rydberg state–auxiliary state transition line, and the associated quadruple magic polarizability $\alpha_v^{(q)}$.

Rydberg state	intermediate state-1	intermediate state-2	$\cos^2 \theta$	$\lambda^{(q)}$ (nm)	Δ (MHz)	$\alpha_v^{(q)}$ (a.u.)
auxiliary state $8P_{1/2, 1/2 }$						
$43S_{1/2, 1/2 }$	$6P_{3/2, 1/2 }$	$5D_{5/2, 5/2 }$	0.4996	1777.6610	2067.04	517.9914
$42D_{3/2, 1/2 }$	$6P_{3/2, 1/2 }$	$5D_{5/2, 5/2 }$	0.4995	1776.7886	22356.16	518.6544
auxiliary state $8P_{3/2, 1/2 }$						
$57S_{1/2, 1/2 }$	$6P_{3/2, 3/2 }$	$5D_{5/2, 1/2 }$	0.1150	1793.4498	771.96	515.2596
$56D_{3/2, 1/2 }$	$6P_{3/2, 3/2 }$	$5D_{5/2, 1/2 }$	0.1150	1793.1735	1497.43	517.6532
$54D_{5/2, 1/2 }$	$6P_{3/2, 3/2 }$	$5D_{5/2, 1/2 }$	0.1145	1794.0898	6549.81	515.3139
auxiliary state $8P_{3/2, 3/2 }$						
$56D_{3/2, 3/2 }$	$6P_{3/2, 3/2 }$	$5D_{5/2, 1/2 }$	0.1153	1792.8876	28171.61	511.6663
$54D_{5/2, 3/2 }$	$6P_{3/2, 3/2 }$	$5D_{5/2, 1/2 }$	0.1138	1794.1316	2652.96	515.3139

condition for a given Rydberg series and given intermediate state tends to have a small θ dependence, i.e., triple magic wavelengths were found for $n = 40 - 70$. Quadruple magic wavelengths, in contrast, are—since they result from the crossing of two triple magic conditions—realized only for very specific n and only in select incidences.

The predicted double, triple, and quadruple magic wavelengths are expected to be useful in, among other things, performing “spectroscopic studies” that can help pin down lifetimes and dipole matrix elements. Initializing the atom in a Rydberg state, the decay out of Rydberg states leads—on short time scales—to state populations that oscillate in time with an overall decay. Their analysis is expected to provide stringent constraints on lifetimes and dipole matrix elements. In addition, the double magic wavelengths might find applications in implementations of different quantum information and quantum metrology protocols.

A natural next step is to extend our study for linearly polarized light to circularly polarized light. Preliminary explorations indicate that elliptically polarized light might offer intriguing advantages. Relatedly, it will be interesting to explore the influence of light sources with a non-Gaussian beam profile, such as vortex light, to confine cesium Rydberg atoms as well as other alkali Rydberg atoms, thereby opening up the possibility of simultaneously trapping mixtures of Rydberg atoms. Such a setting would open the door for leveraging long-range interactions between two Rydberg atoms.

Using n_{eff} , the wavefunction of a Rydberg state can

ACKNOWLEDGEMENT

This work was supported by an award from the W. M. Keck Foundation. We thank Lindsay LeBlanc for discussions on tune-out wavelengths.

Appendix A: Energies, wavefunctions, and dipole matrix elements of Rydberg states

To determine the energies, wavefunctions, and dipole matrix elements of various Rydberg states, we apply quantum defect theory and the Coulomb approximation method [55, 56]. Within quantum defect theory, the principal quantum number n and, correspondingly, the energy levels $\epsilon_{n,L,J}$ of single-valence Rydberg states are parameterized similar to those of the hydrogen atom. Specifically, the energy $\epsilon_{n,L,J}$ of the state nL_J is written in terms of the effective fractional principal quantum number n_{eff} ,

$$\epsilon_{n,L,J} = -\frac{m_r \alpha^2 c^2}{2(n_{\text{eff}})^2}, \quad (\text{A1})$$

where m_r denotes the reduced mass of the atom. The effective principal quantum number is parameterized in terms of the quantum defect parameters $\delta_{L,J,2i}$,

$$n_{\text{eff}} = n - \sum_{i=0}^{\infty} \frac{\delta_{L,J,2i}}{(n - \delta_{L,J,0})^{2i}} \quad (\text{A2})$$

(i is a dummy index). Note that n_{eff} depends on the orbital angular momentum quantum number L and the total angular momentum quantum number J but that the subscripts are suppressed for notational convenience. Table A.1 lists literature values of $\delta_{L,J,2i}$, extracted from experimental data, for various Rydberg series.

be efficiently approximated by the modified Coulomb so-

TABLE A.1. Experimental quantum defect parameters for various Rydberg series of cesium. The entries with superscripts *a*, *b*, *c*, and *d* are taken from Ref. [57], Ref. [58], Ref. [59], and Ref. [60], respectively.

state	$\delta_{L,J,0}$	$\delta_{L,J,2}$	$\delta_{L,J,4}$	$\delta_{L,J,6}$	$\delta_{L,J,8}$
$nS_{1/2}$	4.0493532(4) ^a	0.2391(5) ^a	0.06(10) ^a	11(7) ^a	-209(150) ^a
$nP_{1/2}$	3.5915871(3) ^a	0.36273(16) ^a			
$nP_{3/2}$	3.5590676(3) ^a	0.37469(14) ^a			
$nD_{3/2}$	2.47545(2) ^b	0.0099(40) ^b	-0.43324 ^b	-0.96555 ^b	-16.9464 ^b
$nD_{5/2}$	2.4663144(6) ^a	0.01381(15) ^a	-0.392(12) ^a	-1.9(3) ^a	
$nF_{5/2}$	0.03341537(70) ^c	-0.2014(16) ^c	0.28953 ^d	-0.2601 ^d	
$nF_{7/2}$	0.0335646(13) ^c	-0.2052(29) ^c			

lutions [61]. This approach has previously been shown to yield accurate polarizabilities for alkali atoms [35, 62]. For Rydberg states, the solution to the radial part of the Schrödinger equation that is regular in the $r \rightarrow \infty$ limit (r denotes the distance of the valence electron from the core) and accounts for the orbital angular momentum barrier and Coulomb potential reads [61]

$$R_{n_{\text{eff}},L}(r) = \frac{1}{[a_0 n_{\text{eff}}^2 \Gamma(n_{\text{eff}} + L - 1) \Gamma(n_{\text{eff}} - L)]^{1/2}} \times \frac{W_{n_{\text{eff}},L+1/2}(y)}{W_{n_{\text{eff}},L+1/2}(y)}, \quad (\text{A3})$$

where $W_{n_{\text{eff}},L+1/2}(y)$ with $y = 2r/(n_{\text{eff}}a_0)$ denotes the Whittaker function and a_0 the Bohr radius. One can check readily that the radial wavefunction $R_{n_{\text{eff}},L}(r)$ reduces to the well known non-relativistic bound state wavefunction for integer quantum numbers, i.e., for $n_{\text{eff}} = n$ [35]. The radial transition dipole matrix element R_{ki} is given by

$$R_{ki} = \int_{r_0}^{\infty} dr r R_{n_{\text{eff}},k,L_k}(r) R_{n_{\text{eff}},i,L_i}(r), \quad (\text{A4})$$

where the lower integration limit r_0 needs to be chosen sufficiently small to ensure convergence of the results. We find that

$$r_0 = \frac{s n_{\text{eff},k} n_{\text{eff},i} a_0}{n_{\text{eff},k} + n_{\text{eff},i}} \quad (\text{A5})$$

with s around 1/100 yields converged results.

Appendix B: Calculation of polarizability

The Stark shift $\Delta\xi_v$ for an atom or ion with the valence electron in the v -th state is given within second-order time-independent perturbation theory by

$$\Delta\xi_v(\omega) = -\frac{1}{2} \alpha_v(\omega) E^2, \quad (\text{B1})$$

where E and ω are the amplitude and frequency of the external electric field, respectively. In Eq. (B1), $\alpha_v(\omega)$ denotes—as already noted in the main text—the dynamic polarizability of the v -th state; it reduces to the static polarizability in the $\omega \rightarrow 0$ limit. According to Eq. (3.1), $\alpha_v(\omega)$ is composed of the core polarizability $\alpha_v^C(\omega)$, the

valence-core polarizability $\alpha_v^{VC}(\omega)$, and the valence polarizability $\alpha_v^V(\omega)$.

For a Cs atom, the core is obtained by removing the valence electron, i.e., it is the singly-charged Cs⁺ ion. The polarizability of Cs⁺ can be estimated as [21, 63]

$$\alpha_v^C(\omega) = \frac{2}{3} e^2 \times \sum_{ap} \frac{|\langle \Phi_a || d_{\text{DF}} || \Phi_p \rangle \langle \Phi_a || d_{\text{RMBPT}(2)} || \Phi_p \rangle| (\epsilon_p - \epsilon_a)}{(\epsilon_p - \epsilon_a)^2 - \omega^2}, \quad (\text{B2})$$

where a runs over all occupied core orbital configurations and p represents all virtual orbitals with appropriate symmetries with respect to the core orbitals. The matrix elements $\langle \Phi_a || d_{\text{DF}} || \Phi_p \rangle$ and $\langle \Phi_a || d_{\text{RMBPT}(2)} || \Phi_p \rangle$ are reduced dipole matrix elements at the Dirac-Fock (DF) and the second-order relativistic many-body perturbation theory (RMBPT(2)) levels, respectively [21, 63]. Figure B.1 shows that the core polarizability varies slowly

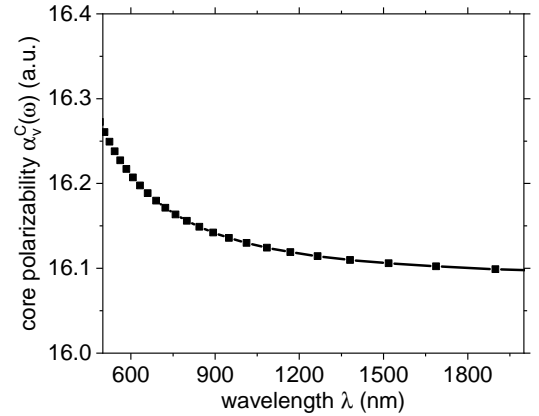


FIG. B.1. Core polarizability $\alpha_v^C(\omega)$ of Cs⁺ as a function of the wavelength λ . It can be seen that the wavelength dependence or, equivalently, the frequency dependence of $\alpha_v^C(\omega)$ is negligible.

with the wavelength of the light and approximately reaches its asymptotic value at the largest wavelength considered, i.e., around $\lambda = 2,000$ nm.

Since the core electrons are tightly bound to the nucleus, the presence of the valence electron provides a

very small change to the core polarizability. Specifically, $\alpha_v^{VC}(0)$ is -0.47 a.u. for the ground state of Cs [64]. Since $|\alpha_v^{VC}(0)|$ is very small and essentially independent of ω , we neglect the ω dependency of $\alpha_v^{VC}(\omega)$ [64, 65]. Moreover, $\alpha_v^{VC}(0)$ is approximately zero for the low-lying excited states considered in this work [64]; correspondingly, we use $\alpha_v^{VC}(\omega) = 0$ throughout for the low-lying excited and Rydberg states.

For linearly polarized light, the valence polarizability $\alpha_v^V(\omega)$ is given by a weighted sum of the scalar polarizability $\alpha_{v,J}^{(0)}(\omega)$ and the tensor polarizability $\alpha_{v,J}^{(2)}(\omega)$ [66–70],

$$\alpha_v^V(\omega) = \alpha_{v,J}^{(0)}(\omega) + \frac{3 \cos^2 \theta - 1}{2} \frac{3M_J^2 - J(J+1)}{J(2J-1)} \alpha_{v,J}^{(2)}(\omega). \quad (\text{B3})$$

The definition of the angle θ is illustrated in Fig. 2. The scalar polarizability has the form

$$\alpha_{v,J}^{(0)}(\omega) = \frac{2}{3(2J+1)} \sum_n d_{nv}, \quad (\text{B4})$$

where $d_{nv} = \frac{e^2 |\langle \psi_v || d || \psi_n \rangle|^2 \omega_{nv}}{\omega_{nv}^2 - \omega^2}$, with ω_{nv} denoting the difference between the frequencies ω_n and ω_v of states ψ_n and ψ_v , respectively, $\omega_{nv} = \omega_n - \omega_v$. The tensor polarizability is given by

$$\alpha_{v,J}^{(2)}(\omega) = 4 \sqrt{\frac{5J(2J-1)}{6(J+1)(2J+1)(2J+3)}} \times \sum_n (-1)^{J_n+J} \left\{ \begin{matrix} J & 1 & J_n \\ 1 & J & 2 \end{matrix} \right\} d_{nv}, \quad (\text{B5})$$

where $\left\{ \right\}$ denotes the $6j$ symbol [66].

To obtain the triple and quadruple magic wavelengths, we consider the polarizabilities of the low-lying states $6S_{1/2,|1/2\rangle}$, $6P_{1/2,|1/2\rangle}$, $6P_{3/2,|1/2\rangle}$, $6P_{3/2,|3/2\rangle}$, $5D_{3/2,|1/2\rangle}$, $5D_{3/2,|3/2\rangle}$, $5D_{5/2,|1/2\rangle}$, $5D_{5/2,|3/2\rangle}$, and $5D_{5/2,|5/2\rangle}$. To calculate the polarizability of these low-lying states, we collected matrix elements from Ref. [71] and energies from Ref. [72].

Appendix C: Changing to (J, I_N, F, M_F) basis

The main text presents the magic wavelengths for simultaneously trapping the ground state and a Rydberg state. Throughout, the states were labeled by n , L , J , and M_J ; the nuclear spin I_N and associated projection quantum number M_I were suppressed. Ultracold experiments, however, work with hyperfine states that are labeled by n , L , J , I_N , F , and M_F . In what follows, we account for the hyperfine splitting and estimate, by showing examples, how the magic wavelengths change when one goes from the (J, M_J, I_N, M_I) to the (J, I_N, F, M_F)

basis. At the hyperfine level, the dynamic polarizability of a valence state is given by [73–75]

$$\alpha_v^V(\omega) = \alpha_{v,F}^{(0)}(\omega) + \frac{3 \cos^2 \theta - 1}{2} \frac{3M_F^2 - F(F+1)}{F(2F-1)} \alpha_{v,F}^{(2)}(\omega), \quad (\text{C1})$$

where $\alpha_{v,F}^{(0)}(\omega)$ and $\alpha_{v,F}^{(2)}(\omega)$ denote, respectively, the scalar and tensor polarizabilities at the hyperfine level [note the similarity between Eqs. (C1) and (B4)]. The scalar polarizability does not change under the basis change, i.e., $\alpha_{v,J}^{(0)}(\omega) = \alpha_{v,F}^{(0)}(\omega)$ [73]. The tensor polarizability, in contrast, changes under the basis change [74, 75],

$$\alpha_{v,F}^{(2)}(\omega) = (-1)^{J+F+I_N} \left\{ \begin{matrix} F & J & I_N \\ J & F & 2 \end{matrix} \right\} \times \sqrt{\frac{F(2F-1)(2F+1)}{(2F+3)(F+1)}} \times \sqrt{\frac{(2J+3)(2J+1)(J+1)}{J(2J-1)}} \alpha_{v,J}^{(2)}(\omega). \quad (\text{C2})$$

Since I_N is equal to $7/2$ for ^{133}Cs , the ground state splits into the $F = 3$ and $F = 4$ manifolds. To illustrate the effect of the basis change, Fig. C.1(a) shows the dynamic polarizabilities of the $6S_{J=1/2, F=4, M_F}$ ground states (M_F can take the values $-4, -3, \dots, 4$) and of the $6P_{J=3/2, F=5, M_F}$ low-lying excited states (M_F can take the values $-5, -4, \dots, 5$) at $\theta = 0$. As noted above, the polarizabilities of the $6S_{J=1/2, F=4, M_F}$ states with different M_F are identical. For the $6P_{J=3/2, F=5, M_F}$ states, the polarizabilities move further away from the resonance line as $|M_F|$ increases from 0 to 5. As a result, the magic wavelengths for the low-lying state $6P_{J=3/2, F=5, M_F}$ and the ground state vary by around 220 nm as the magnitude $|M_F|$ of the projection quantum number that characterizes the low-lying excited state changes [the black box in Fig. C.1(a) highlights the behavior].

Figure C.1(b) considers the polarizabilities of the $F = 4$ ground states and the $45D_{J=3/2, F=5, M_F}$ Rydberg states. Similar to the low-lying excited state in Fig. C.1(a), the polarizability of the Rydberg states is shown for $|M_F| = 0$ to 5 for $\theta = 0$. It can be seen that the magic wavelength changes comparatively little with $|M_F|$. Specifically, the magic wavelength increases by about 0.1 nm as $|M_F|$ changes from 0 to 5 [the black box in Fig. C.1(b) highlights the behavior]. The tiny shift suggests that the tabulated double magic wavelength predictions, calculated by using the (J, M_J, I_N, M_I) basis provide a reliable starting point for locating double magic wavelengths experimentally. This conclusion does not only hold for the $45D_{J=3/2, F=5, M_F}$ Rydberg states but for the entire Rydberg series, other auxiliary states, as well as other Rydberg series.

Now we tune θ , considering the intermediate state $6P_{J=3/2, F=5, M_F=5}$ as an example. We find

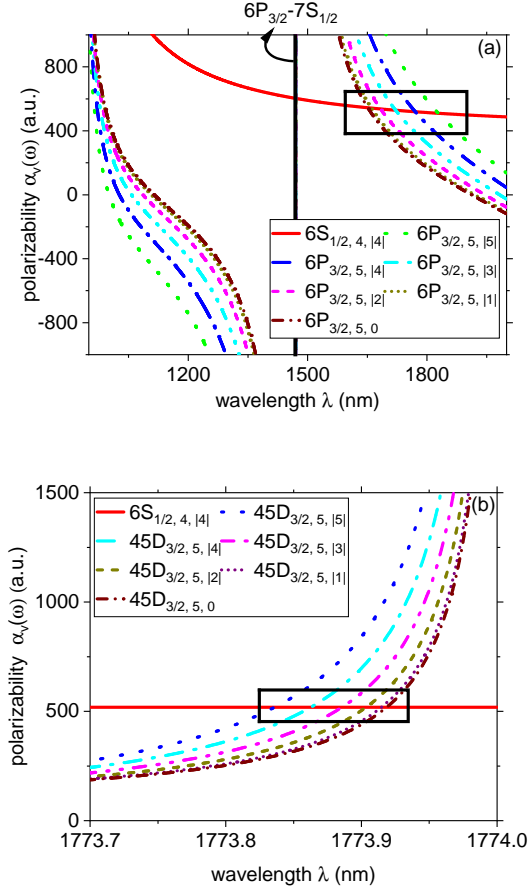


FIG. C.1. Dynamic polarizability $\alpha_v(\omega)$ of (a) the $6S_{J=1/2, F=4, M_F=4}$ ground state (red solid line) and the $6P_{J=3/2, F=5, M_F}$ low-lying excited state (“diving lines”), and (b) the $6S_{J=1/2, F=4, M_F=4}$ ground state (red solid line) and the $45D_{J=3/2, F=5, M_F}$ Rydberg state (“diving lines”) for $\theta = 0$. The “diving lines” show the polarizability of the different $|M_F|$ states for $F = 5$ (see legend). The black boxes draw the readers’ attention to how the magic wavelengths between the ground state and the (a) low-lying excited states and (b) Rydberg states vary with $|M_F|$. The solid black vertical line in (a) indicates the resonance line.

that the ground state and the intermediate state $6P_{J=3/2, F=5, M_F=5}$ exhibit the essentially same ac-Stark shift for $\cos^2 \theta = 0.62$ over the shown wavelength range (the polarizability of the intermediate state $6P_{J=3/2, F=5, M_F=5}$ varies appreciably with θ). Using $\cos^2 \theta = 0.62$, Fig. C.2 shows the dynamic polarizabilities of the ground state $6S_{J=1/2, F=4, M_F=4}$, the intermediate state $6P_{J=3/2, F=5, M_F=5}$, and the Rydberg states $45D_{J=3/2, F=5, M_F}$ with $|M_F| = 0 - 5$. As expected, the polarizability of the $45D_{J=3/2, F=5, M_F}$ states depends weakly on $|M_F|$. The black box in Fig. C.2 highlights the triple magic wavelengths for simultaneous trapping of the ground state, the intermediate state $6P_{J=3/2, F=5, M_F=5}$, and the $45D_{J=3/2, F=5, M_F}$ Rydberg states.

-
- [1] F. Robicheaux, D. W. Booth, and M. Saffman, Theory of long-range interactions for rydberg states attached to hyperfine-split cores, *Phys. Rev. A* **97**, 022508 (2018).
 - [2] T. F. Gallagher, *Rydberg Atoms*, Cambridge Monographs on Atomic, Molecular and Chemical Physics (Cambridge University Press, 1994).
 - [3] M. Saffman, T. G. Walker, and K. Mølmer, Quantum information with rydberg atoms, *Rev. Mod. Phys.* **82**, 2313 (2010).
 - [4] Y. Sun, Suppression of high-frequency components in off-resonant modulated driving protocols for rydberg-blockade gates, *Phys. Rev. Appl.* **20**, L061002 (2023).
 - [5] V. Buchemavari, S. Omanakuttan, Y.-Y. Jau, and I. Deutsch, Entangling quantum logic gates in neutral atoms via the microwave-driven spin-flip blockade, *Phys. Rev. A* **109**, 012615 (2024).
 - [6] C. S. Adams, J. D. Pritchard, and J. P. Shaffer, Rydberg atom quantum technologies, *Journal of Physics B: Atomic, Molecular and Optical Physics* **53**, 012002 (2019).
 - [7] M. Saffman, Quantum computing with atomic qubits and rydberg interactions: progress and challenges, *Journal of Physics B: Atomic, Molecular and Optical Physics* **49**, 202001 (2016).
 - [8] S. Zeytinoğlu and S. Sugiura, Error-robust quantum signal processing using rydberg atoms, *Phys. Rev. Res.* **6**, 013003 (2024).
 - [9] D. Malz and J. I. Cirac, Few-body analog quantum simulation with rydberg-dressed atoms in optical lattices, *PRX Quantum* **4**, 020301 (2023).

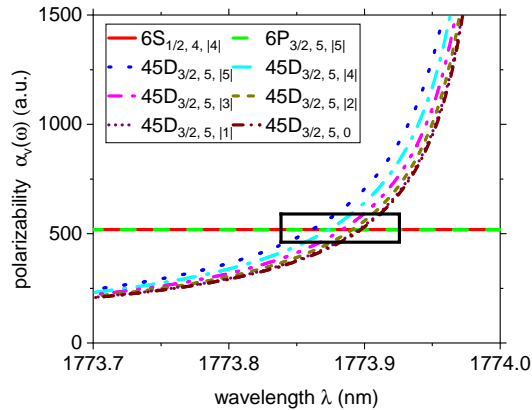


FIG. C.2. Dynamic polarizability $\alpha_v(\omega)$ of the $6S_{J=1/2, F=4, M_F=4}$ ground state (red solid line), the $6P_{J=3/2, F=5, M_F=5}$ low-lying excited state (green dashed line), and the $45D_{J=3/2, F=5, M_F}$ Rydberg state ("diving lines") for $\cos^2\theta = 0.62$. The "diving lines" show the polarizability of the different $|M_F|$ states for $F = 5$ (see legend). The black boxes draw the readers' attention to how the triple magic wavelengths vary with $|M_F|$.

- [10] W. Lee, M. Kim, H. Jo, Y. Song, and J. Ahn, Coherent and dissipative dynamics of entangled few-body systems of rydberg atoms, *Phys. Rev. A* **99**, 043404 (2019).
- [11] J. Zeiher, R. van Bijnen, P. Schauß, S. Hild, J.-y. Choi, T. Pohl, I. Bloch, and C. Gross, Many-body interferometry of a rydberg-dressed spin lattice, *Nature Physics* **12**, 1095 (2016).
- [12] H. Bernien, S. Schwartz, A. Keesling, H. Levine, A. Omran, H. Pichler, S. Choi, A. S. Zibrov, M. Endres, M. Greiner, V. Vuletić, and M. D. Lukin, Probing many-body dynamics on a 51-atom quantum simulator, *Nature* **551**, 579 (2017).
- [13] V. Bharti, S. Sugawa, M. Mizoguchi, M. Kunimi, Y. Zhang, S. de Léséleuc, T. Tomita, T. Franz, M. Weidemüller, and K. Ohmori, Picosecond-scale ultrafast many-body dynamics in an ultracold rydberg-excited atomic mott insulator, *Phys. Rev. Lett.* **131**, 123201 (2023).
- [14] O. Firstenberg, C. S. Adams, and S. Hofferberth, Non-linear quantum optics mediated by rydberg interactions, *Journal of Physics B: Atomic, Molecular and Optical Physics* **49**, 152003 (2016).
- [15] X. Huo, J. F. Chen, J. Qian, and W. Zhang, Interaction-enhanced transmission imaging with rydberg atoms, *Phys. Rev. A* **105**, 012817 (2022).
- [16] I. I. Beterov, I. I. Ryabtsev, D. B. Tretyakov, and V. M. Entin, Quasiclassical calculations of blackbody-radiation-induced depopulation rates and effective lifetimes of rydberg ns , np , and nd alkali-metal atoms with $n \leq 80$, *Phys. Rev. A* **79**, 052504 (2009).
- [17] M. D. Lukin, M. Fleischhauer, R. Cote, L. M. Duan, D. Jaksch, J. I. Cirac, and P. Zoller, Dipole blockade and quantum information processing in mesoscopic atomic ensembles, *Phys. Rev. Lett.* **87**, 037901 (2001).
- [18] T. Xia, M. Lichtman, K. Maller, A. W. Carr, M. J. Piotrowicz, L. Isenhower, and M. Saffman, Randomized benchmarking of single-qubit gates in a 2d array of neutral-atom qubits, *Phys. Rev. Lett.* **114**, 100503 (2015).
- [19] M. Endres, H. Bernien, A. Keesling, H. Levine, E. R. Anschuetz, A. Krajenbrink, C. Senko, V. Vuletic, M. Greiner, and M. D. Lukin, Atom-by-atom assembly of defect-free one-dimensional cold atom arrays, *Science* **354**, 1024 (2016), <https://www.science.org/doi/pdf/10.1126/science.aah3752>.
- [20] K. E. Laidig and R. F. W. Bader, Properties of atoms in molecules: Atomic polarizabilities, *The Journal of Chemical Physics* **93**, 7213 (1990), https://pubs.aip.org/aip/jcp/article-pdf/93/10/7213/18989285/7213.1_online.pdf.
- [21] J. Mitroy, M. S. Safronova, and C. W. Clark, Theory and applications of atomic and ionic polarizabilities, *Journal of Physics B: Atomic, Molecular and Optical Physics* **43**, 202001 (2010).
- [22] R. Grimm, M. Weidemüller, and Y. B. Ovchinnikov, Optical dipole traps for neutral atoms (Academic Press, 2000) pp. 95–170.
- [23] K. C. Younge, S. E. Anderson, and G. Raithel, Adiabatic potentials for rydberg atoms in a ponderomotive optical lattice, *New Journal of Physics* **12**, 023031 (2010).
- [24] R. J. P. T. de Keijzer, O. Tse, and S. J. J. M. F. Kokkelmans, Recapture probability for antitrapped rydberg states in optical tweezers, *Phys. Rev. A* **108**, 023122 (2023).
- [25] S. E. Anderson, K. C. Younge, and G. Raithel, Trapping rydberg atoms in an optical lattice, *Phys. Rev. Lett.* **107**, 263001 (2011).
- [26] L. Li, Y. O. Dudin, and A. Kuzmich, Entanglement between light and an optical atomic excitation, *Nature* **498**, 466 (2013).
- [27] D. Barredo, V. Lienhard, P. Scholl, S. de Léséleuc, T. Boulier, A. Browaeys, and T. Lahaye, Three-dimensional trapping of individual rydberg atoms in ponderomotive bottle beam traps, *Phys. Rev. Lett.* **124**, 023201 (2020).
- [28] P. Xu, X. He, J. Wang, and M. Zhan, Trapping a single atom in a blue detuned optical bottle beam trap, *Opt. Lett.* **35**, 2164 (2010).
- [29] J. T. Wilson, S. Saskin, Y. Meng, S. Ma, R. Dilip, A. P. Burgers, and J. D. Thompson, Trapping alkaline earth rydberg atoms optical tweezer arrays, *Phys. Rev. Lett.* **128**, 033201 (2022).
- [30] H. Katori, T. Ido, and M. Kuwata-Gonokami, Optimal design of dipole potentials for efficient loading of sr atoms, *Journal of the Physical Society of Japan* **68**, 2479 (1999), <https://doi.org/10.1143/JPSJ.68.2479>.
- [31] J. Ye, H. J. Kimble, and H. Katori, Quantum state engineering and precision metrology using state-insensitive light traps, *Science* **320**, 1734 (2008), <https://www.science.org/doi/pdf/10.1126/science.1148259>.
- [32] M. Saffman and T. G. Walker, Analysis of a quantum logic device based on dipole-dipole interactions of optically trapped rydberg atoms, *Phys. Rev. A* **72**, 022347 (2005).
- [33] E. A. Goldschmidt, D. G. Norris, S. B. Koller, R. Wyllie, R. C. Brown, J. V. Porto, U. I. Safronova, and M. S. Safronova, Magic wavelengths for the 5s–18s transition in rubidium, *Phys. Rev. A* **91**, 032518 (2015).
- [34] J. Bai, S. Bai, X. Han, Y. Jiao, J. Zhao, and S. Jia, Precise measurements of polarizabilities of cesium ns rydberg

- states in an ultra-cold atomic ensemble, *New Journal of Physics* **22**, 093032 (2020).
- [35] V. A. Yerokhin, S. Y. Buhmann, S. Fritzsche, and A. Surzhykov, Electric dipole polarizabilities of rydberg states of alkali-metal atoms, *Phys. Rev. A* **94**, 032503 (2016).
- [36] J. Bai, S. Liu, J. He, and J. Wang, Towards implementation of a magic optical-dipole trap for confining ground-state and rydberg-state cesium cold atoms, *Journal of Physics B: Atomic, Molecular and Optical Physics* **53**, 155302 (2020).
- [37] T. Topcu and A. Derevianko, Possibility of triple magic trapping of clock and rydberg states of divalent atoms in optical lattices, *Journal of Physics B: Atomic, Molecular and Optical Physics* **49**, 144004 (2016).
- [38] R.-K. Zhang, J. Jiang, C.-Z. Dong, and Y.-B. Tang, Dynamic polarizabilities and triple magic trapping conditions for $5s^2\ ^1s_0 \rightarrow 5s5p\ ^3p_{0,2}$ transitions of cd atoms (2024), [arXiv:2403.05898 \[physics.atom-ph\]](https://arxiv.org/abs/2403.05898).
- [39] W. R. Johnson, *Atomic Structure Theory* (Springer Berlin, Heidelberg, 2007).
- [40] T. F. Gallagher and W. E. Cooke, Interactions of black-body radiation with atoms, *Phys. Rev. Lett.* **42**, 835 (1979).
- [41] R. Song, J. Bai, Y. Jiao, J. Zhao, and S. Jia, Lifetime measurement of cesium atoms using a cold rydberg gas, *Applied Sciences* **12**, 10.3390/app12052713 (2022).
- [42] T. Lei, S. Gu, Z. Weng, and X. Zeng, Measurement of the polarizabilities of n2d rydberg states of cesium, *Zeitschrift für Physik D Atoms, Molecules and Clusters* **34**, 139 (1995).
- [43] J. Zhao, H. Zhang, Z. Feng, X. Zhu, L. Zhang, C. Li, and S. Jia, Measurement of polarizability of cesium nd state in magneto-optical trap, *Journal of the Physical Society of Japan* **80**, 034303 (2011), <https://doi.org/10.1143/JPSJ.80.034303>.
- [44] Supplemental material, .
- [45] M. Ortiz and J. Campos, Lifetime measurements of 7p levels of cs(i) by means of laser excitation, *Journal of Quantitative Spectroscopy and Radiative Transfer* **26**, 107 (1981).
- [46] J. Marek and K. Niemax, The influence of collisions of xe atoms on the lifetime of atomic states of cs, *Journal of Physics B: Atomic and Molecular Physics* **9**, L483 (1976).
- [47] J. Marek and M. Ryschka, Lifetime measurements of f-levels of cs using partially superradiant population, *Physics Letters A* **74**, 51 (1979).
- [48] J. Marek, Radiative lifetime of the 8s, 9s and 7d levels of csi, *Physics Letters A* **60**, 190 (1977).
- [49] W. S. Neil and J. B. Atkinson, Lifetimes of some excited s and d states of cs i, *Journal of Physics B: Atomic and Molecular Physics* **17**, 693 (1984).
- [50] J. Marek, Study of the time-resolved fluorescence of the cs-xe molecular bands, *Journal of Physics B: Atomic and Molecular Physics* **10**, L325 (1977).
- [51] C. Tuchendler, A. M. Lance, A. Browaeys, Y. R. P. Sortais, and P. Grangier, Energy distribution and cooling of a single atom in an optical tweezer, *Phys. Rev. A* **78**, 033425 (2008).
- [52] H.-P. Breuer and F. Petruccione, *The Theory of Open Quantum Systems* (Oxford University Press, 2007).
- [53] L. J. LeBlanc and J. H. Thywissen, Species-specific optical lattices, *Phys. Rev. A* **75**, 053612 (2007).
- [54] A. Ratkuta, P. D. Gregory, A. D. Innes, A. J. Matthies, L. A. McArd, J. M. Mortlock, M. S. Safronova, S. L. Bromley, and S. L. Cornish, Measurement of the tune-out wavelength for ^{133}Cs at 880 nm, *Phys. Rev. A* **104**, 052813 (2021).
- [55] M. J. Seaton, Quantum defect theory, *Reports on Progress in Physics* **46**, 167 (1983).
- [56] W. van Wijngaarden and J. Li, Polarizabilities of cesium s, p, d, and f states, *Journal of Quantitative Spectroscopy and Radiative Transfer* **52**, 555 (1994).
- [57] J. Deiglmayr, H. Herburger, H. Saßmannshausen, P. Jansen, H. Schmutz, and F. Merkt, Precision measurement of the ionization energy of cs i, *Phys. Rev. A* **93**, 013424 (2016).
- [58] C.-J. Lorenzen and K. Niemax, Quantum defects of the n2p1/2,3/2 levels in 39k i and 85rb i, *Physica Scripta* **27**, 300 (1983).
- [59] J. Bai, R. Song, J. Fan, Y. Jiao, J. Zhao, S. Jia, and G. Raithel, Quantum defects of nF_J levels of cs rydberg atoms, *Phys. Rev. A* **108**, 022804 (2023).
- [60] K.-H. Weber and C. J. Sansonetti, Accurate energies of ns, np, nd, nf, and ng levels of neutral cesium, *Phys. Rev. A* **35**, 4650 (1987).
- [61] D. R. Bates, A. Damgaard, and H. S. W. Massey, The calculation of the absolute strengths of spectral lines, *Philosophical Transactions of the Royal Society of London. Series A, Mathematical and Physical Sciences* **242**, 101 (1949), <https://royalsocietypublishing.org/doi/pdf/10.1098/rsta.1949.0006>.
- [62] W. Van Wijngaarden, Scalar and tensor polarizabilities of low lying s, p, d, f and g states in rubidium, *Journal of Quantitative Spectroscopy and Radiative Transfer* **57**, 275 (1997).
- [63] A. Bhowmik, N. N. Dutta, and S. Majumder, Tunable magic wavelengths for trapping with focused laguerre-gaussian beams, *Phys. Rev. A* **97**, 022511 (2018).
- [64] S. Singh, K. Kaur, B. K. Sahoo, and B. Arora, Comparing magic wavelengths for the $6s^2\ ^1S_{1/2} - 6p^2\ ^1P_{1/2,3/2}$ transitions of cs using circularly and linearly polarized light, *Journal of Physics B: Atomic, Molecular and Optical Physics* **49**, 145005 (2016).
- [65] M. S. Safronova, U. I. Safronova, and C. W. Clark, Magic wavelengths, matrix elements, polarizabilities, and lifetimes of cs, *Phys. Rev. A* **94**, 012505 (2016).
- [66] N. Manakov, V. Ovsianikov, and L. Rapoport, Atoms in a laser field, *Physics Reports* **141**, 320 (1986).
- [67] B. Arora and B. K. Sahoo, State-insensitive trapping of rb atoms: Linearly versus circularly polarized light, *Phys. Rev. A* **86**, 033416 (2012).
- [68] B. Arora, M. S. Safronova, and C. W. Clark, Magic wavelengths for the $np - ns$ transitions in alkali-metal atoms, *Phys. Rev. A* **76**, 052509 (2007).
- [69] J. Jiang, L. Jiang, Z. W. Wu, D.-H. Zhang, L.-Y. Xie, and C.-Z. Dong, Angle-dependent magic wavelengths for the $4s_{1/2} \rightarrow 3d_{5/2,3/2}$ transitions of Ca^+ ions, *Phys. Rev. A* **99**, 032510 (2019).
- [70] A. Bhowmik, N. N. Dutta, and S. Das, Role of vector polarizability induced by a linearly polarized focused laguerre-gaussian light: applications in optical trapping and ultracold spinor mixture, *The European Physical Journal D* **76**, 139 (2022).
- [71] P. Barakhshan, A. Marrs, A. Bhosale, B. Arora, R. Eigenmann, and M. S. Safronova, *Portal for High-Precision Atomic Data and Computation* (version 2.0), University of Delaware, Newark, DE, USA,

- URL:<https://www.udel.edu/atom> (February 2022).
- [72] A. Kramida, Yu. Ralchenko, J. Reader, and and NIST ASD Team, NIST Atomic Spectra Database (ver. 5.11), [Online]. Available: <https://physics.nist.gov/asd> [2024, February 28]. National Institute of Standards and Technology, Gaithersburg, MD. (2023).
- [73] P. Rosenbusch, S. Ghezali, V. A. Dzuba, V. V. Flambaum, K. Beloy, and A. Derevianko, ac stark shift of the cs microwave atomic clock transitions, *Phys. Rev. A* **79**, 013404 (2009).
- [74] J. Kaur, S. Singh, B. Arora, and B. K. Sahoo, Annexing magic and tune-out wavelengths to the clock transitions of the alkaline-earth-metal ions, *Phys. Rev. A* **95**, 042501 (2017).
- [75] A. Das, A. Bhowmik, N. N. Dutta, and S. Majumder, Many-body calculations and hyperfine-interaction effect on dynamic polarizabilities at the low-lying energy levels of y^{2+} , *Phys. Rev. A* **102**, 012801 (2020).